processes

MDPI

Article

Pyrolysis Behavior, Char Structure Evolution, and Kinetics Characteristics of Oil Shale Under N_2 and CO_2 Atmospheres

Qi Liu [1,2], Qing Wang [1,2,*], Zhichao Wang [1,2], Jingru Bai [1,2], Shuai Guo [1] and Chang Xing [3,*]

[1] School of Energy and Power Engineering, Northeast Electric Power University, Jilin 132012, China
[2] Engineering Research Centre of Oil Shale Comprehensive Utilization, Ministry of Education, Northeast Electric Power University, Jilin 132012, China
[3] School of Energy Science and Engineering, Harbin Institute of Technology, Harbin 150001, China
* Correspondence: rlx888@126.com (Q.W.); xingchang@hit.edu.cn (C.X.)

Abstract

This study investigated the effect of replacing N_2 with CO_2 on the pyrolysis behavior, char structure evolution, and kinetics of Fushun (FS) and Changji (CJ) oil shales. Non-isothermal thermogravimetric experiments were conducted at 5, 10, 20, and 40 °C·min^{-1} under N_2 and CO_2 atmospheres, and the resulting chars were characterized by FTIR, XPS, BET, and SEM. Kinetic parameters were evaluated using Friedman, FWO, KAS, Starink, and Vyazovkin iso-conversional methods. Both oil shales underwent three stages: moisture release, main organic-matter pyrolysis, and high-temperature mineral decomposition. Increasing the heating rate shifted T_s and T_{max} to higher temperatures and intensified volatile release. At 40 °C·min^{-1}, replacing N_2 with CO_2 increased T_s from 322.6 to 399.3 °C for FS and from 368.1 to 377.3 °C for CJ, while reducing the maximum mass-loss rates to 6.81 and 8.66%·min^{-1}, respectively. N_2 favored pore development, increasing the specific surface areas of FS and CJ chars to 14.1402 and 6.1464 m^2·g^{-1}, whereas CO_2 caused pore blockage in FS char and reduced its surface area to 2.7783 m^2·g^{-1}. XPS showed that CO_2 promoted the formation or preservation of oxygen-containing surface carbon, especially C=O and O–C=O groups. The E_α values first decreased and then increased with conversion and were generally lower in CO_2 than in N_2. The average activation-energy differences between the two atmospheres were 23.5 and 43.2 kJ·mol^{-1} for FS and CJ, respectively. These results provide experimental and kinetic data for modeling primary oil shale pyrolysis and subsequent char combustion and gasification under CO_2-rich conditions.

Keywords: oil shale; thermogravimetric analysis; pyrolysis mechanism; char structural evolution; activation energy; mineral transformation

Check for updates

Academic Editor: Mattia Bartoli

Received: 10 June 2026
Revised: 21 July 2026
Accepted: 24 July 2026
Published: 29 July 2026

Copyright: © 2026 by the authors. Licensee MDPI, Basel, Switzerland. This article is an open access article distributed under the terms and conditions of the Creative Commons Attribution (CC BY) license.

1. Introduction

Oil shale is an important unconventional fossil resource with abundant organic matter and mineral constituents. Its organic matter mainly occurs as kerogen embedded within the mineral matrix [1–3]. China has widely distributed oil shale resources, with representative deposits located in Fushun, Huadian, and Changji. Among them, Fushun oil shale has a long history of development, whereas Changji oil shale has considerable resource potential, making both important for unconventional energy exploitation and regional energy supplementation [3–6]. However, the direct thermal utilization of oil shale is often limited by low combustion efficiency, strong ash-related effects, and complex pollutant formation mechanisms [3,7]. A deeper understanding of oil shale thermal conversion

and its controlling factors is thus essential for improving its efficient and clean utilization. Recent studies indicate that oil shale research is increasingly shifting from conventional retorting toward controlled heating, in situ conversion, catalytic conversion, and coupled heat-transfer and transport modeling. Particular attention has been paid to the effects of heating rate, pore–fracture evolution, energy-transfer efficiency, and mineral–organic interactions on conversion behavior and product recovery [8–10].

Pyrolysis is a precursor stage in oil shale combustion and gasification. During heating, kerogen first undergoes softening, cracking, and condensation, releasing volatiles and forming shale-oil precursors, pyrolysis gases, and residual char. The pore structure, surface functional groups, and mineral composition of the resulting char then affect its reactivity in subsequent combustion or gasification [11–14]. Because organic matter and minerals are strongly coupled in oil shale, its pyrolysis usually involves overlapping multistage reactions, including low-temperature moisture release, medium-temperature main organic-matter pyrolysis, and high-temperature decomposition of carbonate and other minerals [12,14]. Therefore, TG–DTG curves alone cannot fully reveal the conversion mechanism of oil shale pyrolysis; char structural characterization and kinetic analysis are also required.

In oxy-fuel combustion and other CO_2-rich thermal conversion processes, CO_2 is commonly used as the principal diluent instead of N_2 [15,16]. Owing to differences in density, volumetric heat capacity, thermal conductivity, radiative properties, and molecular diffusivity, replacing N_2 with CO_2 may alter particle-scale heat and mass transfer and consequently affect the temperature history and devolatilization behavior of oil shale [15–17]. In addition to these physical effects, CO_2 may participate in chemical reactions at elevated temperatures. It can react with residual carbon through the Boudouard reaction, particularly in the presence of catalytically active minerals, and its partial pressure may modify the decomposition behavior of carbonate minerals. Therefore, the mass loss observed under CO_2 may reflect the combined effects of primary organic-matter pyrolysis, secondary char conversion, and mineral transformations. These coupled physical and chemical effects can further influence char pore development, surface chemistry, and the apparent activation energy of the overall conversion process [18–20].

Previous studies have separately examined the combustion and utilization characteristics of oil shale, atmosphere-dependent pyrolysis behavior, char physicochemical properties, and pyrolysis kinetics. Research on oil shale combustion has shown that its high ash content, complex mineral composition, and strong organic–mineral association substantially affect conversion efficiency, pollutant formation, and ash behavior [6,17]. Other studies have demonstrated that the pyrolysis atmosphere influences mass-loss characteristics, product distribution, residual-char conversion, and kinetic parameters [11,14,18,19]. Meanwhile, char-characterization studies have revealed atmosphere-induced changes in surface functional groups, carbon species, pore characteristics, and morphology, which may affect the subsequent reactivity of the chars [20–23]. Recent integrated studies combining thermogravimetric analysis, evolved-gas or product characterization, kinetic evaluation, and mechanistic interpretation have further linked kerogen bond cleavage, gas evolution, mineral composition, and conversion pathways [24–26]. Nevertheless, systematic relationships among atmosphere-dependent heat and mass transfer, mineral-associated char evolution, and conversion-dependent kinetic parameters remain insufficiently established.

Kinetic analysis is also necessary for interpreting the multistep pyrolysis behavior of oil shale. Because oil shale pyrolysis involves overlapping processes such as weak-bond cleavage, volatile release, aromatic condensation, char conversion, and mineral transformation, a single global kinetic parameter is insufficient to describe the overall reaction process. Iso-conversional methods can evaluate the conversion-dependent activation energy without assuming a fixed reaction model, making them suitable for complex solid-fuel pyrolysis

systems [24–34]. Therefore, combining differential, linear integral, and nonlinear integral iso-conversional methods can improve the reliability of kinetic interpretation.

More specifically, several issues remain insufficiently clarified. First, systematic comparisons of different oil shales under N_2 and CO_2 atmospheres are still limited, especially for samples with distinct organic–mineral characteristics. Second, the coupling relationships among atmosphere-dependent heat and mass transfer, mineral composition, char surface chemistry, pore morphology, and activation-energy evolution have not been fully established. Third, because organic matter and minerals are strongly coupled in oil shale, the sample-dependent response to CO_2 remains unclear. Therefore, it is necessary to integrate macroscopic pyrolysis behavior, microscopic char structural evolution, and multi-method kinetic analysis to clarify the role of CO_2 in oil shale pyrolysis.

Accordingly, FS and CJ oil shales were selected as two representative Chinese oil shales with different organic–mineral characteristics. Non-isothermal pyrolysis experiments were conducted at different heating rates under N_2 and CO_2 atmospheres to compare their TG–DTG profiles, pyrolysis characteristic parameters, and volatile-release behavior. Pyrolysis chars were subsequently prepared in a tube furnace under the two atmospheres. Although oil shale pyrolysis produces liquid, gaseous, and solid products, this study focuses on pyrolysis char because the residual char determines the subsequent combustion and gasification behavior. The char structure, surface functional groups, pore accessibility, and mineral interactions directly influence reaction pathways and conversion efficiency under CO_2-containing atmospheres. Therefore, systematic characterization of pyrolysis char is essential for understanding the mechanism of atmosphere-dependent thermal conversion. FTIR, XPS, BET, and SEM analyses were performed to characterize changes in char functional groups, surface carbon species, pore structure, and micro-morphology. In addition, Friedman, FWO, KAS, Starink, and Vyazovkin iso-conversional methods were used to evaluate conversion-dependent activation energy. The novelty of this work lies in integrating macroscopic pyrolysis behavior, mineral-related char structural evolution, and multi-method kinetic analysis to clarify how CO_2 substitution modifies oil shale pyrolysis. This integrated approach reveals the mechanistic differences between N_2 and CO_2 atmospheres and provides experimental and kinetic data for modeling primary pyrolysis and subsequent combustion/gasification processes under CO_2-rich conditions.

2. Materials and Methods

2.1. Experimental Samples and Basic Properties

This study focused on two representative Chinese oil shales, Fushun (FS) and Changji (CJ). Both deposits have abundant reserves and have been exploited on a large scale. Fushun and Changji oil shales were selected because they represent two typical Chinese oil shale resources with different geological backgrounds and organic–mineral characteristics. FS oil shale has a long history of exploitation, whereas CJ oil shale represents an important resource in Xinjiang. Their differences in organic matter enrichment and mineral composition provide an appropriate basis for evaluating the influence of atmosphere on oil shale pyrolysis behavior and char evolution.

The samples were prepared through the following procedure: bulk oil shale was first crushed using a hand hammer to a particle size below 30 mm. The samples were then milled in a coal grinder and sieved to collect the fraction passing through a 100-mesh sieve. The sieved samples were dried at 40 °C until constant weight to remove surface moisture and obtain air-dried samples. The dried samples were stored at room temperature in a thermostatic desiccator to preserve their condition before proximate and ultimate analyses and subsequent characterization. Photographs of the raw block samples and the prepared

powder samples of FS and CJ oil shales are provided in Figure 1 to illustrate the sample appearance and preparation procedure.



(**a**) raw FS oil shale (**b**) raw CJ oil shale

(**c**) FS oil shale powder (**d**) CJ oil shale powder

Figure 1. Photographs of raw and prepared oil shale samples: (**a**) raw FS oil shale; (**b**) raw CJ oil shale; (**c**) prepared FS powder passing through a 100-mesh sieve; (**d**) prepared CJ powder passing through a 100-mesh sieve.

Table 1 summarizes the proximate and ultimate analysis data for the FS and CJ oil shale samples, as reported in our study [17]. Both samples show typical high-ash characteristics: the ash contents of FS and CJ are 77.26% and 79.15%, respectively. Such high ash contents indicate that inorganic minerals dominate the fuel matrix, while combustible organic matter is limited, resulting in a lower heat-release capacity than that of conventional coal. The volatile contents of FS and CJ are 17.93% and 17.61%, respectively, indicating similar amounts of pyrolysable components. The fixed-carbon contents are low, only 2.66% for FS and 1.82% for CJ, further highlighting their low-carbon fuel characteristics.

The ultimate analysis further supports this feature. Carbon is the major organic element, accounting for 12.35% and 14.41% in FS and CJ, respectively. The hydrogen contents are relatively low, at 2.37% and 1.98%, while the nitrogen contents are both below 1%. The oxygen contents are also limited, at 4.52% for FS and 1.43% for CJ. Notably, CJ contains slightly more carbon and significantly less oxygen than FS, suggesting a somewhat

higher organic-matter enrichment and potentially more favorable heat-release behavior during thermal reactions. This difference is also reflected in the higher heating value (HHV): FS has an HHV of 4661 kJ·kg^{-1}, whereas CJ reaches 5223 kJ·kg^{-1}, indicating a higher heat-release potential per unit mass for CJ. Meanwhile, the sulfur contents of both samples are below 1%, implying a limited potential for sulfur oxide emissions during combustion.

Table 1. Proximate and ultimate analyses of FS and CJ oil shales (wt%, air-dried basis) [17].

Oil Shale	Proximate Analysis				Ultimate Analysis					HHV [c]
	M	A	V	FC	C	H	N	O [a]	S_t [b]	
FS	2.15	77.26	17.93	2.66	12.35	2.37	0.82	4.52	0.53	4661
CJ	1.42	79.15	17.61	1.82	14.41	1.98	0.96	1.43	0.66	5223

ad: air-dried basis; [a]: by difference; [b]: total sulfur; [c]: higher heating value, kJ·kg^{-1}. M: moisture; A: ash; V: volatile matter; FC: fixed carbon.

To further clarify the inorganic composition of the two oil shales, the oxide compositions of ashes derived from the raw FS and CJ oil shales were summarized based on XRF analysis, as shown in Table 2. Because the XRF results are expressed on an ash basis, they mainly reflect the inorganic constituents of the oil shale samples. Both FS and CJ ashes are dominated by SiO_2, with contents of 55.30 and 55.70 wt%, respectively, indicating that silicate minerals are the major inorganic components. Compared with CJ ash, FS ash contains higher Al_2O_3 and Fe_2O_3 contents, suggesting a stronger contribution from aluminosilicate and iron-bearing minerals. In contrast, CJ ash shows much higher CaO and MgO contents than FS ash, indicating a higher abundance of Ca- and Mg-bearing inorganic components. This difference provides a compositional basis for interpreting the more pronounced high-temperature mineral-related mass loss and the stronger atmosphere-dependent structural evolution of CJ oil shale. It should be noted that XRF provides the bulk oxide composition of the ash rather than direct identification of crystalline mineral phases.

Table 2. Oxide composition of ashes derived from raw FS and CJ oil shales determined by XRF (wt%, ash basis) [17].

Ash	SiO_2	Al_2O_3	Fe_2O_3	CaO	MgO	SO_3	TiO_2	K_2O	Na_2O	P_2O_5
FS	55.30	22.60	10.90	0.72	1.25	0.77	1.07	1.20	1.14	0.21
CJ	55.70	12.20	6.99	6.14	2.66	1.23	0.54	2.59	2.22	0.52

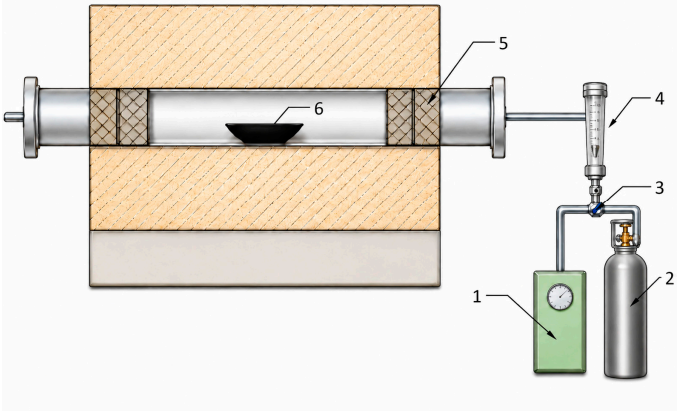
2.2. Experimental Apparatus and Test Conditions

2.2.1. Pyrolysis Experiments and Preparation of Pyrolysis Chars

Oil shale pyrolysis experiments were conducted using a TGA/DSC 1 thermal analyzer (Mettler–Toledo Group, Zurich, Switzerland). For each run, the sample mass was kept at 10 ± 0.1 mg. The samples were heated from 30 to 1000 °C at heating rates of 5, 10, 20, and 40 °C·min^{-1}. High-purity N_2 and CO_2 gases (99.999%; Jihua Northern Ultra-Pure Gas Co., Ltd., Jilin City, China) were used as reaction atmospheres. The gas flow rate was maintained at 50 mL·min^{-1} to ensure a stable atmosphere and comparable heat- and mass-transfer conditions. Each experimental condition was repeated twice to improve reliability.

To further examine the role of pyrolysis atmosphere, FS and CJ pyrolysis chars were prepared in a horizontal tube furnace. Before each experiment, 100 ± 1 mg of FS or CJ oil shale was accurately weighed with a high-precision electronic balance and evenly spread at the center of the heating zone. The heating rate was set to 20 °C·min^{-1} using a PID temperature controller, and heating was stopped immediately after the temperature reached 1000 °C. During heating, high-purity N_2 or CO_2 was continuously introduced

at a volumetric flow rate of 500 mL·min^{-1} to maintain a stable atmosphere in the tube. After pyrolysis, the heating system was turned off, and the furnace was allowed to cool naturally to room temperature under the protective atmosphere. The N_2-derived or CO_2-derived char samples were then collected, sealed, and stored under dry conditions at room temperature for subsequent morphological observation and structural characterization. The tube-furnace experiments were mainly used to prepare char samples for structural characterization. Although the sample mass and gas flow rate differed from those used in TG experiments, the heating rate and final temperature were kept consistent to improve the comparability of heat-treatment conditions. The schematic diagram of the horizontal tube furnace system used for char preparation is shown in Figure 2.



1—fully automatic air source; 2—high-purity N_2 or CO_2; 3—three-way valve; 4—rotameter; 5—pipe plug; 6—corundum crucible.

Figure 2. Schematic diagram of the horizontal tube furnace system used for preparing pyrolysis chars under N_2 and CO_2 atmospheres.

2.2.2. Structural Characterization of Raw Oil Shales and Pyrolysis Chars

The functional groups of the raw oil shales and the chars obtained under N_2 and CO_2 atmospheres were analyzed using a Thermo Nicolet IS 10 FTIR spectrometer (Thermo Electron Scientific Instruments LLC, Madison, WI, USA). The KBr pellet method was used. For each measurement, 1 mg of solid sample was thoroughly mixed with 100 mg of KBr and pressed in a mold at 2 MPa for 8 min. Spectra were collected over 400–4000 cm^{-1} with 64 scans. The assignment of FTIR characteristic peaks was based on previous studies of oil shale and kerogen pyrolysis [20,35]. In this study, FTIR was used mainly to identify the evolution trends of characteristic functional groups. Because oil shale contains abundant inorganic minerals and several absorption bands of organic functional groups overlap with mineral-related bands, FTIR peak intensities were not used for direct quantitative or semi-quantitative determination of functional-group contents. Instead, the FTIR results were interpreted together with XPS C 1s peak-fitting results to evaluate changes in surface chemical structures.

XPS analysis of all samples was carried out using a Thermo ESCALAB 250Xi photoelectron spectrometer (Thermo Fisher Scientific Inc., Waltham, MA, USA). The instrument was operated with a monochromatic Al Kα X-ray source at 150 W, and the base pressure in the analysis chamber was maintained below 5×10^{-8} Pa. Binding energies were calibrated against the C 1s peak at 284.8 eV as an internal reference. Survey spectra were recorded at a pass energy of 100 eV with a step size of 1 eV, whereas high-resolution spectra were acquired at a pass energy of 30 eV with a step size of 0.1 eV. To improve signal stability and surface representativeness, the samples were ground to a particle size of $\leq$0.074 mm and pressed into pellets before XPS analysis.

To examine the textural properties and pore-structure evolution of the two oil shales during pyrolysis in different atmospheres, BET analysis was performed on the raw oil shales and their corresponding char samples. Specific surface area measurements were carried out using a Micromeritics TriStar II 3020 automatic surface area analyzer (Micromeritics Instrument Corporation, Norcross, GA, USA). The specific surface area was determined by the BET method, and the pore-size distribution was derived from the desorption branch using the BJH method. Surface micro-morphology was observed using a JEOL JSM-7610F field-emission scanning electron microscope (JEOL Ltd., Akishima, Tokyo, Japan), with a typical imaging magnification of ×5000. Because the samples had poor electrical conductivity, their surfaces were coated with a thin gold film before testing to improve conductivity and obtain clearer and more stable micrographs.

2.3. Determination of Pyrolysis Characteristic Parameters

Volatile matter content is an important indicator for evaluating oil shale quality. It generally refers to the total amount of gaseous products released from organic-matter pyrolysis when oil shale is heated in the absence of air, and its release behavior directly reflects the pyrolysis reactivity and conversion potential of oil shale. To quantitatively characterize the volatile-release behavior of the two oil shale samples during pyrolysis, a comprehensive volatile-release characteristic index (D value) was introduced to evaluate the release rate and intensity of volatiles. In general, a larger D value indicates a more active overall pyrolysis process and a higher volatile-release rate. The definition and calculation of D in this study follow the methods reported by Kang et al. [18] and Huang et al. [19], as expressed in Equation (1):

$$D = \frac{(dw/dt)_{max}(dw/dt)_{mean}}{T_s T_{max} \Delta T_{1/2}} \quad (1)$$

where T_s is the initial volatile-release temperature (°C), corresponding to the temperature at which the mass-loss rate reaches 0.1 mg·min^{-1} on the DTG curve; $(dw/dt)_{max}$ is the maximum mass-loss rate during volatile release (%·min^{-1}); T_{max} is the temperature corresponding to $(dw/dt)_{max}$ (°C); $(dw/dt)_{mean}$ is the average mass-loss rate during volatile release (%·min^{-1}), defined as the ratio of pyrolysis mass loss to time; and $\Delta T_{1/2}$ is the temperature interval at which $(dw/dt)/(dw/dt)_{max} = 1/2$, namely the half-peak width (°C).

2.4. Kinetic Analysis

Based on the thermogravimetric data, the kinetic characteristics of oil shale pyrolysis under N_2 and CO_2 atmospheres were further investigated. According to the basic Arrhenius rate equation, the kinetic equation for a non-isothermal heterogeneous reaction can be written as:

$$\frac{d\alpha}{dt} = k(T) f(\alpha) \quad (2)$$

where α is the conversion of the sample, t is the reaction time (min), T is the reaction temperature (K), $k(T)$ is the temperature-dependent reaction rate constant, and $f(\alpha)$ is the reaction mechanism function. The conversion α is expressed as:

$$\alpha = \frac{m_0 - m_t}{m_0 - m_f} \quad (3)$$

where m_0 and m_f are the initial and final masses of the sample during the experiment, respectively, and m_t is the sample mass at time t. All mass parameters are expressed in mg. According to the Arrhenius equation, $k(T)$ can be expressed as:

$$k(T) = A\exp\left(-\frac{E}{RT}\right) \tag{4}$$

where $k(T)$ represents the temperature-dependent reaction rate constant, A is the pre-exponential factor, E is the apparent activation energy, R is the universal gas constant, and $f(\alpha)$ represents the reaction model function.

By substituting the Arrhenius expression for $k(T)$ into the general kinetic equation, the reaction rate can be expressed as Equation (5).

$$\frac{d\alpha}{dt} = A\exp\left(-\frac{E}{RT}\right)f(\alpha) \tag{5}$$

where $k(T)$ represents the temperature-dependent reaction rate constant, A is the pre-exponential factor, E is the apparent activation energy, R is the universal gas constant, and $f(\alpha)$ represents the reaction model function.

In non-isothermal thermogravimetric analysis, oil shale is heated at a constant heating rate, $\beta = dT/dt$ (K·min^{-1}). Thus, the reaction rate with respect to temperature can be written as Equation (6).

$$\frac{d\alpha}{dT} = \left(\frac{A}{\beta}\right)\exp\left(-\frac{E}{RT}\right)f(\alpha) \tag{6}$$

For integral iso-conversional analysis, the integral form of the reaction model is expressed as Equation (7).

$$g(\alpha) = \frac{A}{\beta}\int_{T_0}^{T}\exp\left(-\frac{E}{RT}\right)dT \approx \frac{A}{\beta}\int_{0}^{T}\exp\left(-\frac{E}{RT}\right)dT = \frac{AE}{\beta R}P(u) \tag{7}$$

where u denotes the apparent activation-energy term and $P(u)$ is the temperature integral, which can be expressed as Equation (8).

$$P(u) = \int_{\infty}^{u} -\frac{e^{-u}}{\mu^2}du,\ u = \frac{E}{RT} \tag{8}$$

For the Friedman method [27], the logarithmic form of the differential kinetic equation is used. At a fixed conversion α, $f(\alpha)$ remains constant, and the apparent activation energy can be obtained from the slope of the linear relationship between $\ln(\beta d\alpha/dT)$ and $1/T$:

$$\ln\left(\beta\frac{d\alpha}{dT}\right) = \ln[Af(\alpha)] - \frac{E}{RT} \tag{9}$$

For the FWO [28,29] method, the temperature integral is approximated to obtain a linear relationship between $\lg\beta$ and $1/T$ at a fixed conversion α:

$$\lg\beta = \lg\left(\frac{AE}{Rg(\alpha)}\right) - 2.315 - \frac{0.4567E}{RT} \tag{10}$$

The apparent activation energy during the reaction process can then be determined from the slope of the corresponding linear fitting curve.

For the KAS method [30,33], the temperature integral is further transformed into a linear expression involving $\ln\left(\beta_i/T_{\alpha,i}^2\right)$ and $1/T_{\alpha,i}$, where $T_{\alpha,i}$ is the temperature corresponding to a given conversion α at the heating rate β_i:

$$\ln\left(\frac{\beta_i}{T_{\alpha,i}^2}\right) = \ln\left(\frac{AE}{Rg(\alpha)}\right) - \frac{E}{RT} \tag{11}$$

The apparent activation energy can also be obtained from the slope of this linear relationship.

The Starink method [31] improves the approximation of the temperature integral by introducing an empirical exponent of 1.92. The corresponding linear expression is:

$$\ln\left(\frac{\beta_i}{T_{\alpha,i}^{1.92}}\right) = \ln\left(\frac{AE}{Rg(\alpha)}\right) - 1.0008\left(\frac{E_\alpha}{RT_\alpha}\right) \tag{12}$$

Similarly, the apparent activation energy can be calculated from the slope of the corresponding linear fitting curve.

The above expressions provide the basis for the kinetic analysis of oil shale pyrolysis. By combining thermogravimetric data obtained at four heating rates with suitable iso-conversional methods, the activation energy can be evaluated as a function of conversion. Iso-conversional methods are generally classified as integral or differential approaches. Friedman is a differential method, whereas integral iso-conversional methods can be further grouped into linear and nonlinear forms. Traditional linear integral methods, including FWO, KAS, and Starink, use approximate solutions for the temperature integral, which may introduce considerable errors in E_α, particularly when E_α changes markedly with conversion.

To reduce the errors caused by traditional linear iso-conversional methods, the advanced nonlinear integral procedure proposed by Vyazovkin [36–38] was also employed. In this method, the reaction model integral $g(\alpha)$, the pre-exponential factor A, the apparent activation energy E, the gas constant R, and the temperature program $T(t)$ are considered in the time-integral form:

$$g(\alpha) = A\int_0^t \exp\left[-\frac{E}{RT(t)}\right]dt \tag{13}$$

Equation (14) is defined to eliminate the influence of the pre-exponential factor A:

$$J[E_\alpha, T_i(t_\alpha)] = [\frac{g(\alpha)}{A}] = \int_{t_{\alpha-\Delta\alpha}}^{t_\alpha} \exp\left(-\frac{E_\alpha}{RT_i(t)}\right)dt \tag{14}$$

Because the mechanism function $g(\alpha)$ is independent of the heating program, the value of the time integral should be consistent for experiments performed at different heating rates at a given conversion α. For the ith heating program, β_i denotes the corresponding heating rate, $T_{\alpha,i}$ denotes the temperature at conversion α, E_α denotes the apparent activation energy at this conversion, and $I(E_\alpha, T_{\alpha,i})$ represents the corresponding temperature integral. Therefore, for n experiments conducted at different heating rates, the following relationship should hold:

$$\left(\frac{A_\alpha}{\beta_1}\right)I(E_\alpha, T_{\alpha,1}) = \left(\frac{A_\alpha}{\beta_2}\right)I(E_\alpha, T_{\alpha,2}) = \ldots = \left(\frac{A_\alpha}{\beta_n}\right)I(E_\alpha, T_{\alpha,n}) \tag{15}$$

This equality can be expressed as a minimization problem to determine the most appropriate value of E_α. The minimization function is denoted by $\Phi(E_\alpha)$, where i and j represent two different heating programs and n is the total number of heating rates. The function is defined as:

$$\Phi(E_\alpha) = \sum_{i=1}^{n}\sum_{j\neq 1}^{n}\frac{J[E_\alpha, T_i(t_\alpha)]}{J[E_\alpha, T_j(t_\alpha)]} \tag{16}$$

In the Vyazovkin iso-conversional method, integration is performed over short time intervals, and the only assumption is that the apparent activation energy E_α remains constant within each interval. For n experiments conducted at different heating rates, E_α for each interval is obtained by minimizing the function $\Phi(E_\alpha)$ in Equation (16). The minimization

procedure is then repeated at each conversion level α to establish the relationship between E_α and α. By solving the temperature integral through segmented time integration, this method avoids direct temperature-integral approximation and reduces the associated systematic errors [29]. The five iso-conversional kinetic methods used in the subsequent kinetic calculations are summarized in Table 3. For examples of activation energy calculation, please refer to the Supplementary Materials.

Table 3. The five iso-conversional kinetic methods used in this study.

Kinetic Method		Equation	Plot	Slope
Differential method	Friedman	$\ln\left(\frac{d\alpha}{dt}\right)_{\alpha,i} = \ln\left(\beta\frac{d\alpha}{dT}\right)_{\alpha,i} = \ln[A_\alpha f(\alpha)] - \frac{E_\alpha}{RT_{\alpha,i}}$	$\ln\left(\beta\frac{d\alpha}{dT}\right)_{\alpha,i}$ vs. $\frac{1}{T_{\alpha,i}}$	$-\frac{E_\alpha}{R}$
Linear integral method	FWO	$\lg\beta = \lg\left(\frac{AE}{Rg(\alpha)}\right) - 2.315 - \frac{0.4567E}{RT}$	$\ln(\beta_i)$vs. $\frac{1}{T_{\alpha,i}}$	$-1.052\frac{E_\alpha}{R}$
	KAS	$\ln\left(\frac{\beta_i}{T_{\alpha,i}^2}\right) = \ln\left(\frac{AE}{Rg(\alpha)}\right) - \frac{E}{RT}$	$\ln\left(\frac{\beta_i}{T_{\alpha,i}^2}\right)$vs. $\frac{1}{T_{\alpha,i}}$	$-\frac{E_\alpha}{R}$
	Starink	$\ln\left(\frac{\beta_i}{T_{\alpha,i}^{1.92}}\right) = \ln\left(\frac{AE}{Rg(\alpha)}\right) - 1.0008\left(\frac{E_\alpha}{RT_\alpha}\right)$	$\ln\left(\frac{\beta_i}{T_{\alpha,i}^{1.92}}\right)$vs. $\frac{1}{T_{\alpha,i}}$	$-1.0008\frac{E_\alpha}{R}$
Nonlinear integral method	Vyazovkin	$\Phi(E_\alpha) = \sum_{i=1}^{n}\sum_{j\neq1}^{n}\frac{J[E_\alpha, T_i(t_\alpha)]}{J[E_\alpha, T_j(t_\alpha)]}$ $J[E_\alpha, T_i(t_\alpha)] = \int_{t_{\alpha-\Delta\alpha}}^{t_\alpha}\exp\left(-\frac{E_\alpha}{RT_i(t)}\right)dt$	The activation energy E_α is determined by minimizing the $\Phi(E_\alpha)$ function.	

3. Results and Discussion

3.1. Comparison of Thermophysical and Transport Properties of CO_2 and N_2

Figure 3 compares the ratios of thermodynamic, heat-transfer, and mass-transfer parameters of CO_2 to those of N_2 as a function of temperature at 1 atm. As shown in Figure 3a, the density of CO_2 is approximately 1.57 times that of N_2 and changes only slightly with temperature, mainly because of the higher molecular weight of CO_2. In contrast, the C_p and C_v ratios of CO_2 increase gradually with temperature, indicating a stronger heat-capacity contribution from CO_2 in the medium- and high-temperature regions. Because of its higher heat capacity, CO_2 can absorb more reaction heat and reduce the local heating rate, thereby contributing to the thermal dilution effect observed during the early stages of pyrolysis and combustion. Similar heat-transfer effects of CO_2 substitution have been reported in oxy-fuel combustion studies of coal and biomass, where the higher heat capacity of CO_2 results in lower heating rates and delayed volatile release compared with N_2 atmospheres [15,16].

Figure 3b shows that the kinematic viscosity ν and thermal diffusivity α of CO_2 are both markedly lower than those of N_2. In particular, the thermal diffusivity of CO_2 remains lower than that of N_2 over the entire temperature range, indicating weaker heat diffusion in a CO_2 atmosphere. Although the thermal conductivity k of CO_2 gradually approaches and eventually exceeds that of N_2 as temperature increases, its overall thermal diffusivity remains lower because CO_2 has both higher density and higher heat capacity. Therefore, replacing N_2 with CO_2 reduces the efficiency of heat transfer to fuel particles and reactive regions. In addition, the lower kinematic viscosity of CO_2 indicates weaker momentum diffusivity. The variation in dynamic viscosity μ mainly reflects internal gas friction and should not be directly equated with momentum diffusion capacity. The Prandtl number

ratio remains close to 1 with only minor variation, suggesting that the relative balance between momentum and thermal diffusion changes only slightly.

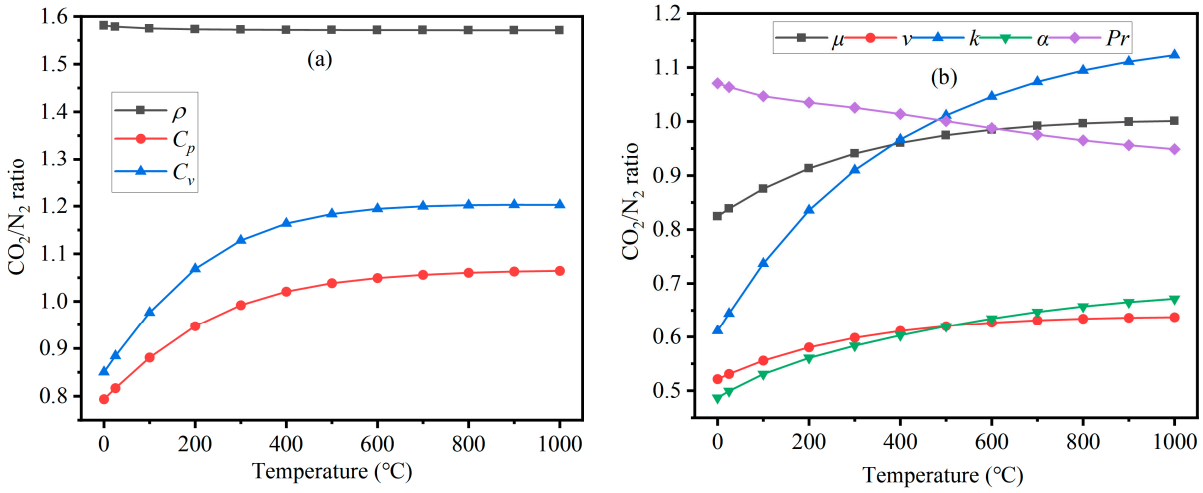


Figure 3. Ratios of thermodynamic and transport properties of CO_2 to those of N_2 as a function of temperature at 1 atm: (**a**) ρ, density; C_p, isobaric heat capacity; C_v, isochoric heat capacity; (**b**) μ, dynamic viscosity; ν, kinematic viscosity; k, thermal conductivity; α, thermal diffusivity; Pr, Prandtl number.

These property differences imply that, under the same external heating conditions, a CO_2 atmosphere provides stronger thermal buffering and a more pronounced heat-transfer lag. This behavior can mainly be explained by two factors. First, the higher heat capacity of CO_2 enables it to absorb more heat, thereby prolonging the time required for the interior of the sample particles to reach the same reaction temperature. Second, the lower thermal diffusivity and weaker mass-transfer ability reduce heat transport into the particles and volatile diffusion outward. Consequently, the macroscopic mass-loss process of oil shale pyrolysis under CO_2 may be characterized by a higher onset temperature, a delayed mass-loss peak, or a lower mass-loss rate. It should be noted that these property effects may differ among oil shale samples. Although FS and CJ have similar organic-matter contents, their mineral compositions and pore structures differ. Therefore, CO_2 affects pyrolysis not only through heat- and mass-transfer effects but also through possible gasification reactions and ash rearrangement at medium and high temperatures. Thus, the difference between N_2 and CO_2 atmospheres is not merely a difference in diluent gas; it can further influence oil shale pyrolysis, char structural evolution, and mass-transfer conditions during subsequent combustion or gasification.

3.2. Pyrolysis Behavior and Characteristic Parameters of Oil Shale

3.2.1. Overall Pyrolysis Process

Figure 4 shows the TG and DTG curves of FS and CJ oil shales under N_2 and CO_2 atmospheres. Both samples exhibit clear multistage mass-loss behavior under the two atmospheres, but their peak shapes and high-temperature mass-loss features differ. Overall, when the heating rate increased from 5 to 40 °C·min^{-1}, the TG and DTG curves shifted toward higher temperatures. This rightward shift is consistent with recent oil shale studies and has generally been attributed to thermal hysteresis and transient internal temperature gradients, which require higher external temperatures to achieve a comparable conversion. Meanwhile, rapid heating compresses devolatilization into a shorter time interval and may limit the occurrence of secondary cracking and mineral-related reactions [8,18,19]. The total mass loss varied only slightly with heating rate, indicating that the heating rate primarily

affects the temperature response and instantaneous pyrolysis rate, while exerting only a limited influence on the final extent of conversion.

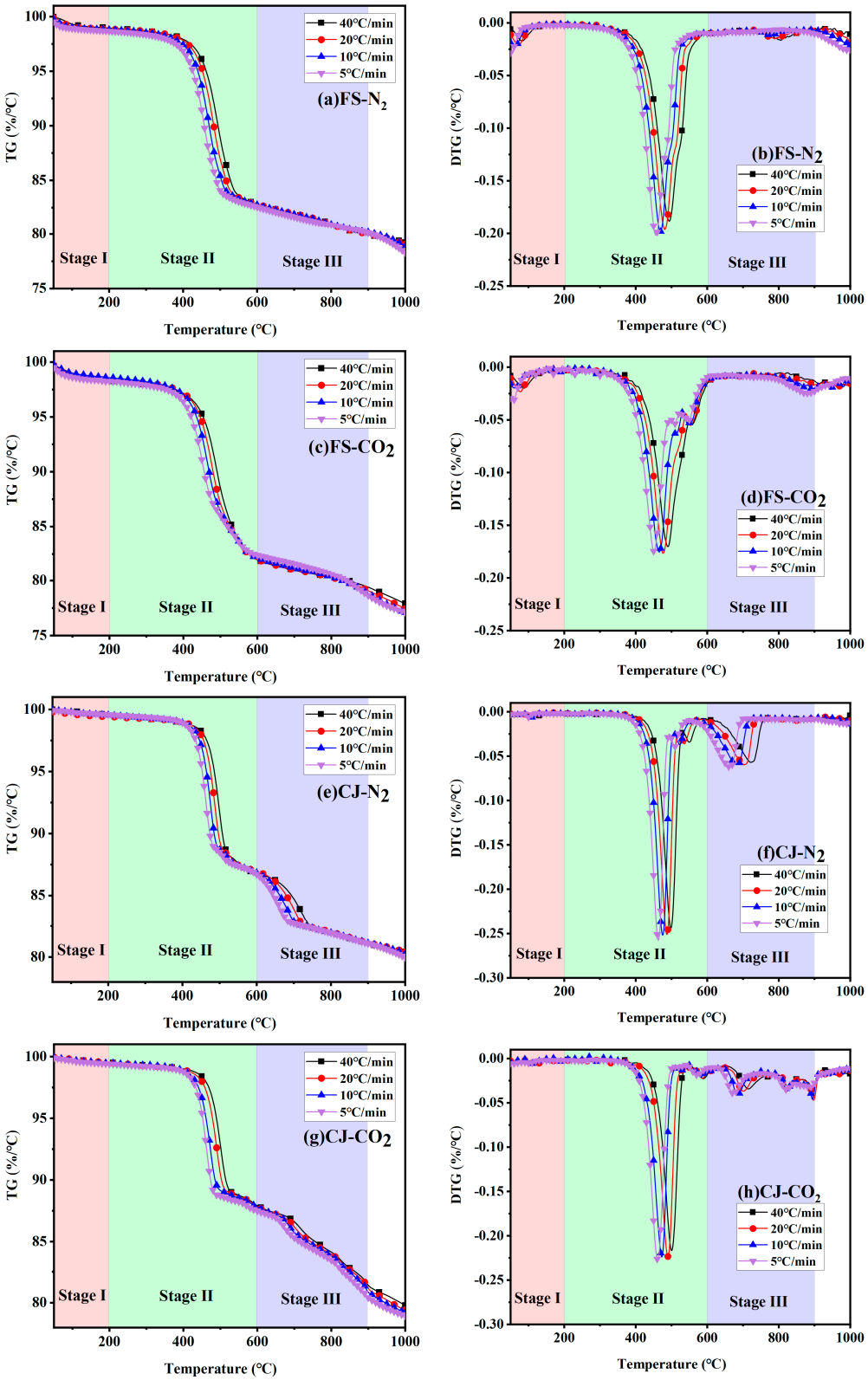


Figure 4. TG–DTG curves of FS and CJ oil shale pyrolysis under N_2 and CO_2 atmospheres: (**a**) FS-N_2 TG, (**b**) FS-N_2 DTG, (**c**) FS-CO_2 TG, (**d**) FS-CO_2 DTG, (**e**) CJ-N_2 TG, (**f**) CJ-N_2 DTG, (**g**) CJ-CO_2 TG, and (**h**) CJ-CO_2 DTG. Stage I, Stage II, and Stage III represent moisture release, main organic-matter pyrolysis, and high-temperature mineral decomposition/transformation, respectively.

The mass-loss behavior of the two oil shales can be divided into three characteristic stages according to the TG–DTG profiles in Figure 4 and previous oil shale pyrolysis studies [14,18,19]. It should be noted that these temperature ranges represent approximate characteristic intervals rather than strict reaction boundaries. Stage I, from 30 to 200 °C, corresponds mainly to slight mass loss caused by the removal of physically adsorbed moisture and weakly bound water. Because no evolved-gas analysis was performed in this study, this assignment is based on the TG–DTG mass-loss characteristics and literature reports rather than direct identification of water species. Stage II, from 200 to 600 °C, corresponds to the main pyrolysis of organic matter, during which kerogen cracking and volatile release are most pronounced. In this stage, the TG curves drop rapidly, and the DTG curves exhibit the main mass-loss peak. Kerogen undergoes softening, cracking, condensation, and volatile release, producing pyrolysis gases, shale-oil precursors, and residual carbonaceous structures. Stage III, from 600 to 900 °C, is associated with high-temperature mineral decomposition/transformation, including carbonate-related transformation and ash-structure rearrangement.

The differences between FS and CJ are mainly reflected in the main pyrolysis peak and the high-temperature mineral decomposition stage. FS shows a relatively concentrated main mass-loss stage, with the DTG curve dominated by a single main peak, indicating concentrated release of organic pyrolysis products. In contrast, CJ exhibits more obvious double-peak or secondary-peak characteristics, suggesting stronger stage separation between organic-matter pyrolysis and mineral decomposition. In particular, CJ shows more pronounced mass loss above 600 °C, indicating a greater contribution from carbonate or other high-temperature-decomposable minerals. As shown in Table 2, CJ ash contains much higher CaO and MgO contents than FS ash, whereas FS ash is richer in Al_2O_3 and Fe_2O_3. The higher CaO and MgO contents of CJ indicate a greater contribution from Ca- and Mg-bearing inorganic components, which are commonly associated with carbonate-related minerals in oil shale. Therefore, the more pronounced mass loss of CJ in the 600–900 °C range can be attributed to carbonate-related decomposition/transformation and high-temperature mineral-phase rearrangement. In contrast, the higher Al_2O_3 content of FS suggests a larger contribution from aluminosilicate minerals, which are relatively more stable during this temperature range. Similar high-temperature mass loss in Estonian oil shale has also been attributed to carbonate mineral decomposition [39]. Recent investigations of Xinjiang oil shale also demonstrated that pyrolysis atmosphere influences volatile release behavior and high-temperature conversion characteristics, which is consistent with the delayed devolatilization observed under CO_2 in the present study [18,19].

3.2.2. Analysis of Pyrolysis Characteristic Parameters

Table 4 summarizes the pyrolysis characteristic parameters of FS and CJ oil shales at different heating rates and in different atmospheres. The $(dw/dt)_{max}$ values are expressed as absolute mass-loss rates. With the heating rate increasing from 5 to 40 °C·min^{-1}, T_s and T_{max} for both oil shales moved to higher-temperature regions. For example, in FS-N_2, T_s increased from 301.3 to 322.6 °C and T_{max} from 456.4 to 494.1 °C. In CJ-N_2, T_s increased from 332.7 to 368.1 °C and T_{max} from 463.4 to 498.1 °C. These numerical variations in T_s and T_{max} further confirm the heating-rate-induced thermal hysteresis discussed in Section 3.2.1. A higher heating rate also favored a more concentrated release of volatiles over a shorter period. Under N_2, the maximum mass-loss rate of FS-N_2 increased from 1.01 to 7.53%·min^{-1}, while the D value rose from 0.33×10^{-7} to 14.93×10^{-7}. For CJ-N_2, the corresponding values increased from 1.28 to 9.75%·min^{-1} and from 0.46×10^{-7} to 19.62×10^{-7}, respectively. Thus, the heating-rate effect is mainly reflected in the shift in characteristic temperatures and the enhancement of instantaneous release intensity.

Table 4. Pyrolysis characteristic parameters of FS and CJ oil shales under two atmospheres.

Sample	Heating Rate (°C·min^{-1})	T_s (°C)	T_{max} (°C)	$(dw/dt)_{max}$ (%·min^{-1})	$(dw/dt)_{mean}$ (%·min^{-1})	$\Delta T_{1/2}$ (°C)	D (10^{-7})
FS-N_2	5	301.3	456.4	1.01	0.30	74.0	0.33
	10	310.6	469.8	1.98	0.64	74.4	1.19
	20	317.6	481.3	3.93	1.37	77.3	4.35
	40	322.6	494.1	7.53	2.41	82.7	14.93
FS-CO_2	5	341.3	451.7	0.87	0.30	87.1	0.19
	10	368.5	466.1	1.74	0.69	88.3	0.80
	20	384.6	477.6	3.52	1.48	86.8	3.27
	40	399.3	490.1	6.81	2.74	90.7	10.52
CJ-N_2	5	332.7	463.4	1.28	0.26	47.1	0.46
	10	340.1	474.5	2.51	0.49	48.7	1.56
	20	359.3	487.3	5.01	0.96	49.3	5.58
	40	368.1	498.1	9.75	1.90	51.5	19.62
CJ-CO_2	5	359.5	460.7	1.13	0.21	52.7	0.28
	10	366.6	472.6	2.23	0.43	52.9	1.06
	20	373.1	490.1	4.46	0.87	52.8	4.04
	40	377.3	500.6	8.66	1.72	54.5	14.51

Regarding the atmospheric effect, CO_2 clearly delayed T_s. At the same heating rate, T_s of FS-CO_2 was consistently higher than that of FS-N_2; for example, it increased from 301.3 to 341.3 °C at 5 °C·min^{-1} and from 322.6 to 399.3 °C at 40 °C·min^{-1}. CJ showed a similar trend, with T_s increasing from 332.7 to 359.5 °C at 5 °C·min^{-1} and from 368.1 to 377.3 °C at 40 °C·min^{-1}. This delay is mainly associated with the higher heat capacity of CO_2, its lower thermal diffusivity, and restricted volatile diffusion [11,14]. However, the influence of CO_2 on T_{max} was not a simple unidirectional increase. For FS, T_{max} under CO_2 was slightly lower than that under N_2; at 40 °C·min^{-1}, FS-N_2 and FS-CO_2 showed T_{max} values of 494.1 and 490.1 °C, respectively. For CJ, T_{max} shifted slightly to higher temperatures at 20 and 40 °C·min^{-1}, increasing from 487.3 and 498.1 °C to 490.1 and 500.6 °C, respectively. This indicates that the effect of CO_2 on the peak temperature is jointly controlled by sample composition, heating rate, and secondary reactions in the medium- and high-temperature regions. Similar CO_2-induced delays in volatile release have been observed in other carbonaceous materials. In coal and biomass pyrolysis, CO_2 generally decreases the apparent devolatilization rate because of its higher heat capacity, thermal buffering effect, and altered mass-transfer behavior compared with N_2 atmospheres [15,16]. However, oil shale differs from these carbonaceous materials because a large fraction of the solid matrix consists of inorganic minerals, which can participate in high-temperature mineral transformation and gas-solid interactions [3,11]. Although the high-pressure supercritical CO_2 conditions used in recent studies differ substantially from the atmospheric-pressure CO_2 atmosphere employed in the present work, these studies provide complementary evidence that CO_2-containing media can affect pyrolysis-product displacement and pore-structure evolution. Supercritical CO_2 has been reported to facilitate the transport of shale-oil and gas products and to modify pore diameter and pore development during organic-rich shale pyrolysis. These findings cannot be directly extrapolated to the present atmospheric-pressure system, but they support the broader interpretation that the influence of CO_2 may involve coupled heat transfer, product transport, and structural evolution rather than the simple replacement of an inert diluent [40].

Regarding reaction intensity, the CO_2 atmosphere generally lowered both the maximum mass-loss rate and the comprehensive pyrolysis characteristic index. At 40 °C·min^{-1},

$(dw/dt)_{max}$ of FS decreased from 7.53%·min^{-1} under N_2 to 6.81%·min^{-1} under CO_2, while the D value decreased from 14.93×10^{-7} to 10.52×10^{-7}. For CJ, $(dw/dt)_{max}$ decreased from 9.75 to 8.66%·min^{-1}, and the D value decreased from 19.62×10^{-7} to 14.51×10^{-7}. At 40 °C·min^{-1}, the decrease in D for CJ was 5.11×10^{-7}, larger than the 4.41×10^{-7} decrease for FS, indicating that CJ was more sensitive to the atmosphere switch. This behavior may be associated with its higher organic carbon content, more pronounced high-temperature mineral decomposition, and the involvement of carbonate-related reactions.

Overall, CO_2 has a dual effect on oil shale pyrolysis. At low temperature and during the early stage of main pyrolysis, it mainly delays macroscopic mass loss and lowers the volatile-release rate through thermal buffering and heat- and mass-transfer lag. At medium and high temperatures, however, CO_2 may participate in char gasification, secondary reactions of volatiles, and mineral-assisted reactions, thereby modifying the mass-loss peak shape, pore structure, and subsequent reaction pathways. Therefore, in CO_2-rich or oxy-fuel combustion environments, primary volatile release from oil shale may be delayed, whereas the char structure and mineral behavior at medium and high temperatures may still strongly affect subsequent combustion or gasification.

3.3. Kinetic Analysis of Oil Shale Pyrolysis

To improve the reliability of the kinetic analysis, five commonly used iso-conversional methods were adopted, namely FWO, KAS, Starink, Friedman, and Vyazovkin. Figure 5 shows the iso-conversional fitting curves obtained by the Starink method for CJ and FS pyrolysis under N_2 and CO_2 atmospheres. The FWO and KAS methods produced similar fitting behavior and are therefore not shown. Figure 6 presents the iso-conversional fitting curves based on the Friedman method. Figures 5 and 6 show that the fitting results from the different iso-conversional methods generally exhibit good linearity, supporting their applicability to the pyrolysis kinetic analysis of FS and CJ oil shales in N_2 and CO_2 atmospheres. The activation-energy values calculated by different methods differ to some extent. Linear integral methods are affected by temperature-integral approximations, differential methods are more sensitive to experimental data fluctuations, and the nonlinear integral Vyazovkin method can reduce approximation errors associated with the temperature integral. Therefore, the Vyazovkin method is more suitable as a key basis for discussing activation-energy trends.

The relationship between E_α and α during pyrolysis of the two oil shales under CO_2 and N_2 atmospheres is shown in Figure 7. Under the same pyrolysis condition, the E_α–α curves obtained by the five iso-conversional methods show generally consistent shapes. Except for the Friedman method, the activation-energy curves calculated by FWO, KAS, Starink, and Vyazovkin overlap well, with only small differences in absolute values, indicating good consistency among the kinetic results. For both oil shales under N_2 and CO_2 atmospheres, the E_α–α curves show a typical trend of an initial decrease, a relatively stable middle region, and a subsequent increase. At low conversion ($\alpha \leq 0.2$), weak-bond cleavage, light volatile release, and active-site formation occur simultaneously, leading to a rapid decrease in E_α. At intermediate conversion ($0.2 \leq \alpha \leq 0.6$), main organic-matter cracking dominates and E_α remains relatively stable, suggesting that this stage is mainly controlled by chemical reactions. At high conversion ($\alpha \geq 0.6$), condensation of the residual aromatic carbon framework, char gasification, pore shrinkage, and mineral decomposition become increasingly important. The resulting increase in diffusion/interfacial resistance causes E_α to rise markedly. Recent kinetic studies of Fushun and Beizao oil shales have likewise reported conversion-dependent apparent activation energies, reflecting the progressive overlap of weak-bond cleavage, primary organic-matter cracking, secondary reactions, aromatic condensation, and mineral-related transformation during heating [24,25]. Ac-

cordingly, the E_α values obtained in the present study should be interpreted as effective apparent energy barriers associated with evolving multistep reaction pathways rather than as a single intrinsic kinetic constant.

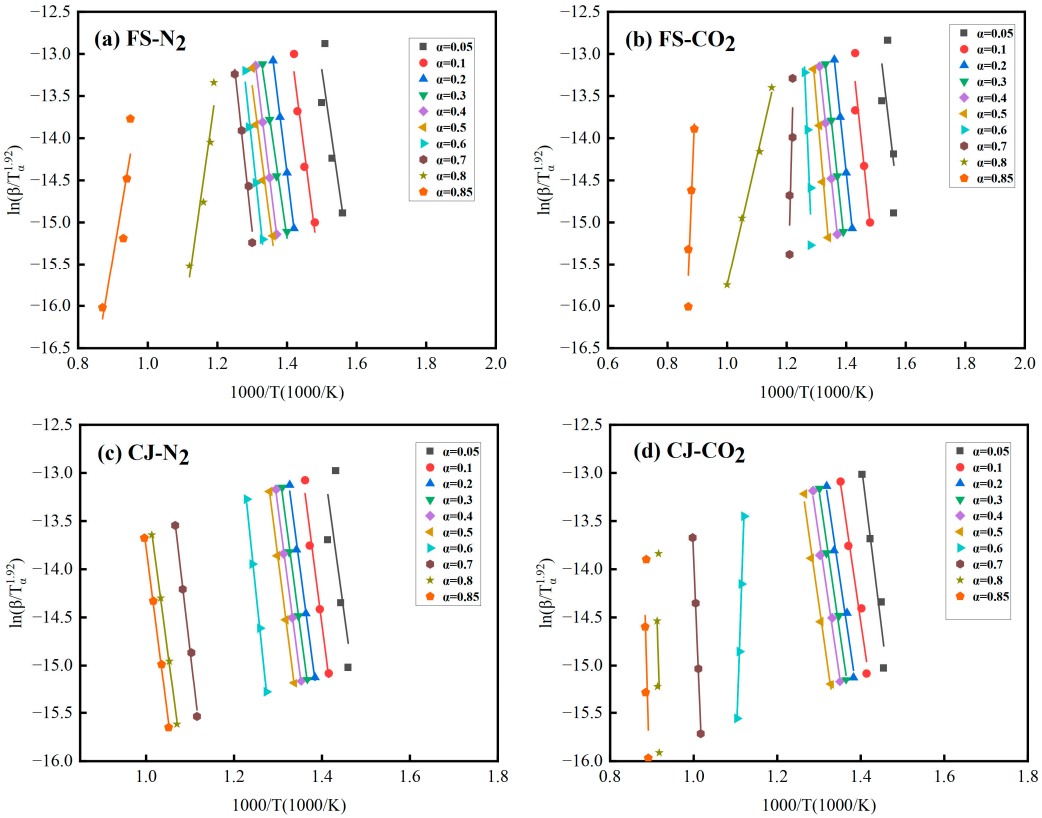


Figure 5. Iso-conversional fitting curves of FS and CJ oil shales under N_2 and CO_2 atmospheres obtained by the Starink method.

Comparison of activation energies under the two atmospheres shows that E_α of both oil shales is generally higher under N_2 than under CO_2. For FS-N_2, E_α varies approximately within 275–370 kJ·mol^{-1}, whereas FS-CO_2 ranges from about 265 to 355 kJ·mol^{-1}. For CJ-N_2, E_α mainly falls within 285–335 kJ·mol^{-1}, while CJ-CO_2 decreases markedly to approximately 240–310 kJ·mol^{-1}. Further comparison shows that the average E_α difference between N_2 and CO_2 is about 43.2 kJ·mol^{-1} for CJ, significantly larger than the approximately 23.5 kJ·mol^{-1} difference for FS. This indicates that CJ is more kinetically sensitive to atmospheric switching. It should be noted that the higher heat capacity and lower heat- and mass-transfer efficiency of CO_2 delay the macroscopic mass-loss process and reduce the apparent pyrolysis rate. However, at medium and high conversions, CO_2 can participate in char gasification, pore formation, and mineral-assisted reactions, introducing parallel low-energy-barrier pathways. Therefore, the E_α values calculated by iso-conversional methods can be lower under CO_2 than under N_2. Previous studies on coal, biomass-derived chars, and oil shale pyrolysis have demonstrated that the effect of CO_2 on apparent activation energy is strongly dependent on conversion stage, fuel composition, mineral characteristics, and gas–solid interactions [8,14,27,31,32]. This result is not inconsistent with the TG–DTG behavior and pyrolysis characteristic parameters discussed above. TG–DTG reflects the macroscopic mass-loss rate and temperature response of pyrolysis, which are strongly affected by heat transfer, diffusion, and atmospheric properties. In contrast, E_α obtained from iso-conversional methods reflects the effective reaction energy barrier at a given conversion and is jointly affected by reaction pathways, char gasification, mineral catalysis, and pore-structure evolution.

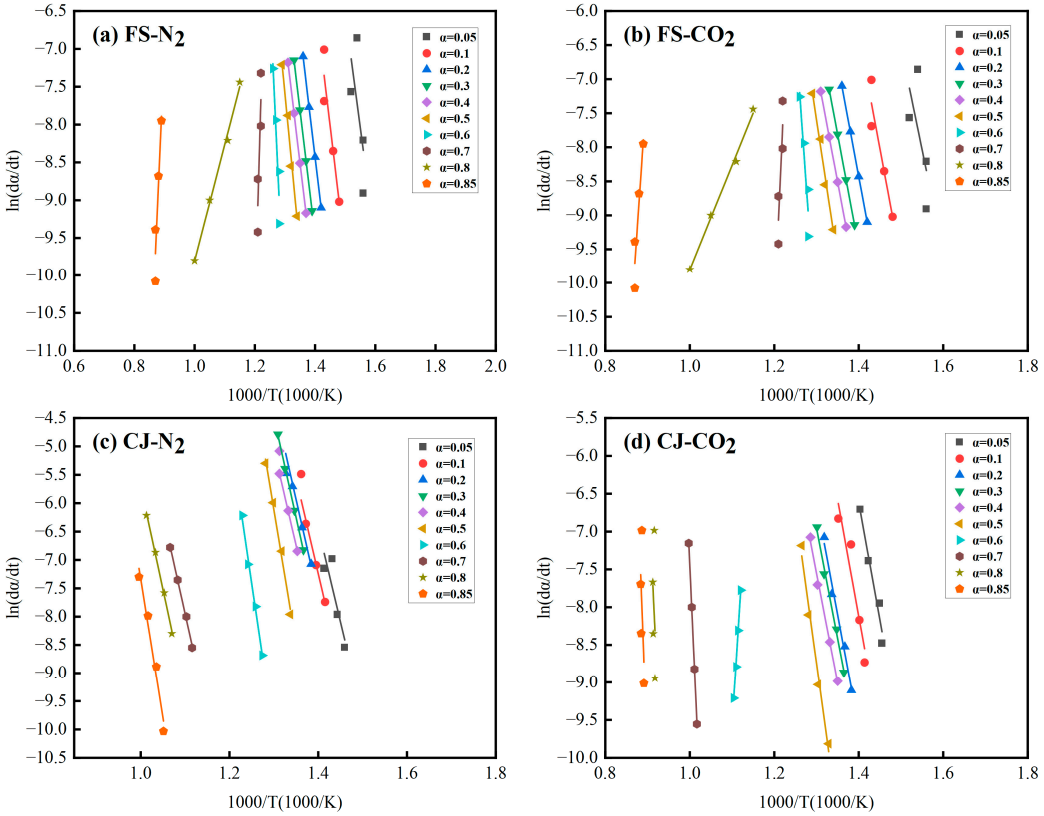


Figure 6. Iso-conversional fitting curves of FS and CJ oil shales under N_2 and CO_2 atmospheres obtained by the Friedman method.

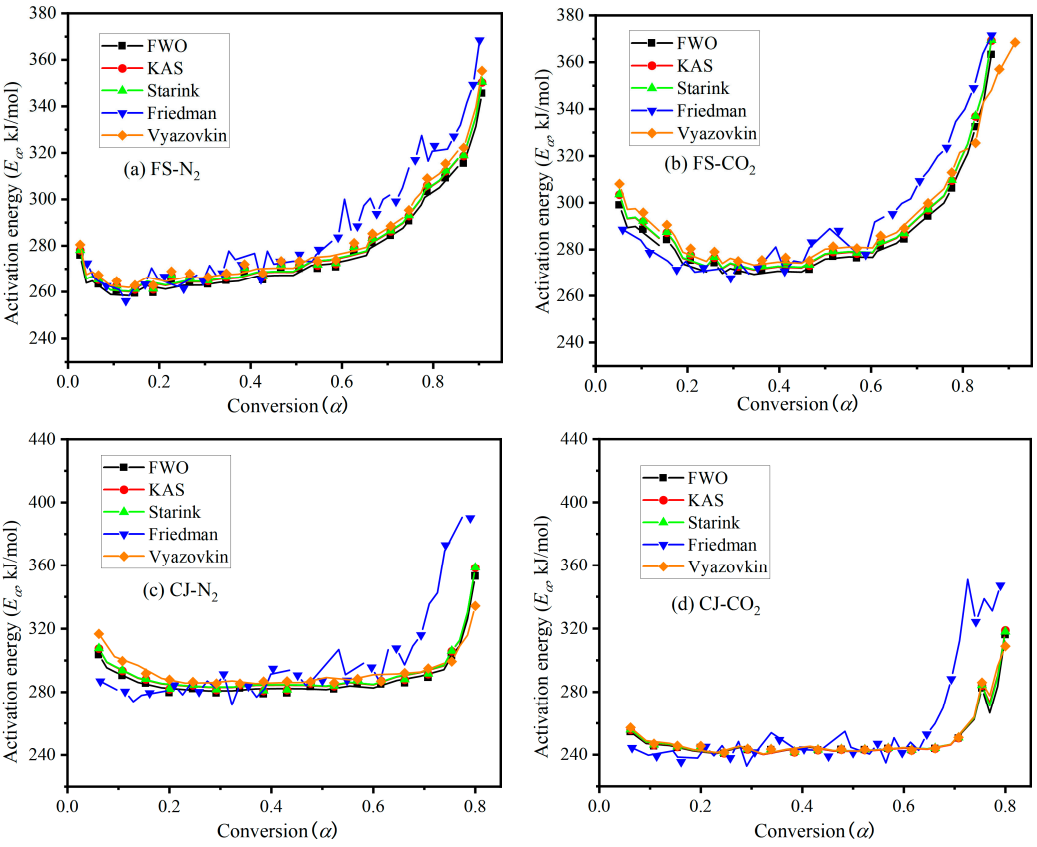


Figure 7. Activation energy of FS and CJ oil shale pyrolysis under N_2 and CO_2 atmospheres.

The kinetic differences between the two samples are closely related to their basic composition and structural evolution. N_2 is essentially inert, and pyrolysis under N_2 mainly depends on the cleavage and rearrangement of aromatic frameworks and cross-linking bonds, such as C–C and C–O bonds. This process can readily induce secondary polycondensation and pore blockage, making the rate more strongly controlled by the intrinsic chemical energy barrier and resulting in higher E_α. At medium and high temperatures, CO_2 may participate in char conversion through gasification reactions such as $C + CO_2 \rightarrow 2CO$, and may be coupled with carbonate-related decomposition, ash migration, and pore restructuring. These processes can promote new pore formation, expose active sites, and introduce parallel low-energy-barrier pathways. The larger decrease in E_α for CJ under CO_2 may be associated with stronger carbonate participation, pore-size refinement, and small-pore formation. However, at high α, ash-shell densification, pore shrinkage, and increased tortuosity may strengthen internal diffusion/interfacial control, causing E_α to rise at later stages. Thus, the effect of CO_2 on pyrolysis kinetics is strongly stage-dependent: at low temperature, it mainly acts through thermal buffering and mass-transfer delay, whereas at medium and high temperatures it modifies the effective energy barrier through gasification, mineral-assisted reactions, and pore restructuring.

Overall, the pyrolysis kinetics of FS and CJ under N_2 and CO_2 atmospheres exhibit multistep reaction characteristics, with the controlling mechanism changing with conversion. Although the CO_2 atmosphere lowers the macroscopic mass-loss rate and D value, it can reduce the apparent activation energy at medium and high conversions through gasification and mineral-assisted effects. These results indicate that, when evaluating oil shale reactivity in CO_2-rich or oxy-fuel combustion environments, TG-DTG peak values or a single activation-energy value should not be used alone. Instead, characteristic temperatures, mass-loss rates, pore structure, surface functional groups, and E_α–α curves should be considered together.

3.4. Evolution of Functional Groups and Surface Chemical Structures During Pyrolysis

3.4.1. FTIR Analysis of Functional-Group Evolution

Figure 8 shows the FTIR spectra of raw FS and CJ oil shales and their chars obtained under N_2 and CO_2 atmospheres. Overall, both oil shales contain characteristic absorption bands associated with O–H, aliphatic C–H, aromatic C=C, C–O, and Si–O–Si groups, but their peak intensities and peak-position combinations differ markedly. Previous FTIR studies of oil shale usually assign the bands near 2920–2850 cm^{-1} to aliphatic C–H stretching vibrations, the band near 1600 cm^{-1} to aromatic C=C skeletal vibrations, and the bands near 1000–1100 cm^{-1} mainly to C–O or Si–O–Si stretching vibrations [14,32].

It should be noted that the FTIR analysis in this study was used mainly for qualitative comparison of functional-group evolution. Because the two oil shales contain high mineral contents, several absorption bands partly overlap, such as O–H bands from moisture or clay minerals and C–O/Si–O–Si bands from organic oxygen-containing structures and silicate minerals. In addition, the peak intensity of KBr-pellet FTIR spectra can be affected by sample dispersion, matrix effects, and baseline correction. Therefore, the FTIR spectra were not used to calculate quantitative peak-area ratios. Instead, the FTIR observations were combined with XPS C 1s peak-fitting results to obtain a more reliable interpretation of surface chemical evolution.

Specifically, raw FS exhibits strong O–H stretching bands at 3699 and 3621 cm^{-1}, indicating notable contributions from clay-mineral hydroxyls, such as those in kaolinite, and adsorbed water. The aliphatic C–H bands at 2927 and 2851 cm^{-1} indicate the presence of alkyl side chains. The aromatic C=C skeletal vibration at 1609 cm^{-1} is relatively distinct, suggesting a certain degree of aromaticity in FS organic matter. Strong absorption bands at

1032 and 1086 cm^{-1} are mainly related to Si–O–Si stretching, reflecting pronounced silicate mineral characteristics. In comparison, raw CJ shows more prominent alkyl C–H bands at 2926 and 2852 cm^{-1}, whereas the aromatic C=C band at 1611 cm^{-1} is relatively weak, indicating a higher proportion of aliphatic components and slightly lower aromaticity in its organic matter. In addition, the C–O-related absorptions near 1165, 1092, and 1037 cm^{-1} are more evident in CJ, suggesting greater involvement of oxygen-containing structures such as ether bonds and carboxylic acid derivatives in its organic framework.

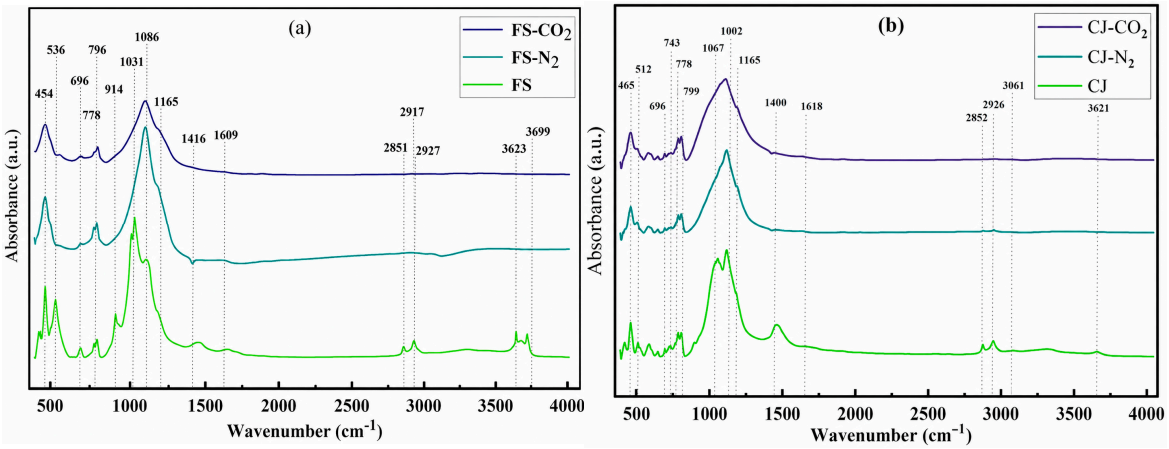


Figure 8. FTIR spectra of raw FS and CJ oil shales and their pyrolysis chars: (**a**) FS samples; (**b**) CJ samples.

After pyrolysis, both oil shales show weakened aliphatic C–H bands and relatively enhanced aromatic structures, indicating that aliphatic side-chain cracking and aromatization of residual carbon structures are major structural evolution features during pyrolysis. For FS, the aliphatic C–H bands at 2927 and 2851 cm^{-1} are clearly weakened in the char obtained under N_2, whereas the aromatic C=C absorption at 1609 cm^{-1} is enhanced. This indicates that inert pyrolysis mainly promotes aliphatic side-chain cleavage, volatile release, and enrichment of aromatic carbon frameworks. Under CO_2, FS-CO_2 char shows enhanced C–O/Si–O–Si-related absorptions near 1032 and 1165 cm^{-1} and stronger O–H absorption near 3621 cm^{-1}, while the aromatic C=C absorption further intensifies. This suggests that CO_2-involved gas–solid reactions may promote the formation or retention of oxygen-containing structures in the char.

The functional-group evolution of CJ is more strongly characterized by the consumption of aliphatic structures. After pyrolysis under N_2, the aliphatic C–H bands at 2926 and 2852 cm^{-1} are greatly weakened, the aromatic C=C band at 1611 cm^{-1} is enhanced, and the C–O absorptions in the 1165 and 1092 cm^{-1} regions slightly decrease. These changes indicate the transformation of CJ from an aliphatic-rich structure toward a more aromatized and carbonized structure. Under CO_2, the overall intensities of organic absorption bands in CJ-CO_2 char decrease markedly, and both the C–O stretching and aromatic C=C bands become much weaker. This suggests that the bulk organic matter underwent more extensive cracking, gasification, and ash–framework reconstruction. Therefore, FTIR changes in FS mainly reflect oxygen-containing structure retention and aromatic-structure enhancement, whereas CJ shows stronger aliphatic-structure consumption and char-framework rearrangement. For subsequent combustion or gasification, the loss of aliphatic C–H indicates substantial consumption of volatile-prone structures, while changes in aromatic carbon frameworks and oxygen-containing functional groups will influence oxygen adsorption capacity, CO_2 gasification reactivity, and interfacial reaction sites of the char. Because FTIR mainly reflects bulk vibrational features and is affected by overlapping organic and mineral-related bands,

the changes in oxygen-containing carbon species were further evaluated using XPS C 1s peak fitting in the following section.

3.4.2. XPS Analysis of Carbon Forms

Figure 9 and Table 5 summarize the high-resolution C 1s peak-fitting results for raw FS and CJ oil shales and their corresponding chars. Based on the binding energies, the C 1s spectra were resolved into four components: C–C/C–H, C–O/C–OH, C=O, and O–C=O. The C–C/C–H component at approximately 284.8 eV is attributed to aliphatic and aromatic carbon, while C–O/C–OH at approximately 286.3 eV is associated with alcoholic hydroxyl and ether groups. The C=O component at approximately 287.5 eV is assigned to carbonyl groups, and O–C=O at approximately 289.0 eV corresponds to carboxyl and ester groups [41].

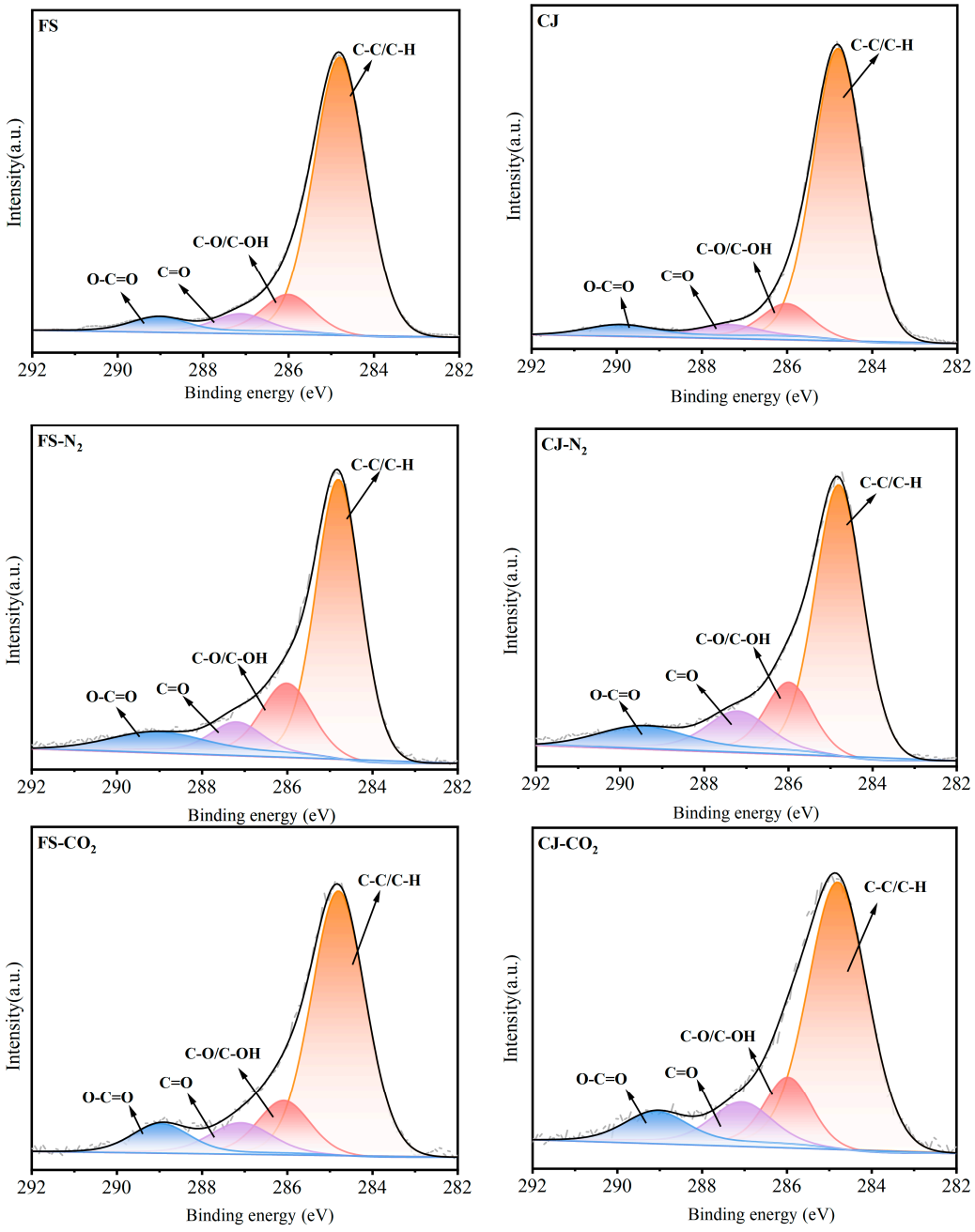


Figure 9. XPS C 1s spectra of raw FS and CJ oil shales and their pyrolysis chars.

Table 5. C 1s peak assignments and relative contents of raw FS and CJ oil shales and their pyrolysis char.

Elemental Peak	Functional Group	Binding Energy (eV)	Raw	Char-N_2	Char-CO_2
FS C 1s	C–C/C–H	284.80	81.72%	70.04%	68.35%
	C–O/C–OH	286.30	12.04%	19.32%	18.33%
	C=O	287.50	1.99%	4.13%	5.91%
	O–C=O	289.00	4.25%	6.52%	7.41%
CJ C 1s	C–C/C–H	284.80	88.1%	68.13%	65.44%
	C–O/C–OH	286.30	8.03%	20.43%	22.12%
	C=O	287.50	1.06%	4.48%	5.02%
	O–C=O	289.00	2.73%	6.97%	7.42%

At the raw-sample stage, the two oil shales show clear differences in surface carbon forms. In raw FS, C–C/C–H accounts for 81.72%, while C–O/C–OH, C=O, and O–C=O account for 12.04%, 1.99%, and 4.25%, respectively, giving a total oxygen-containing carbon fraction of 18.28%. In raw CJ, the C–C/C–H fraction is higher, at 88.10%, whereas C–O/C–OH, C=O, and O–C=O account for 8.03%, 1.06%, and 2.73%, respectively, giving a total oxygen-containing carbon fraction of 11.82%. This indicates that the surface of raw CJ is dominated by a more reduced carbon framework, while the surface of FS contains relatively more oxygen-containing functional groups and polar structures. It should be noted that FTIR reflects bulk vibrational features, whereas XPS reflects surface chemical states; therefore, both should be considered together when evaluating oxygen-containing structures.

After pyrolysis, both oil shales exhibited a lower C–C/C–H fraction and a higher proportion of oxygen-containing carbon species. For FS under N_2, C–C/C–H decreases from 81.72% to 70.04%, C–O/C–OH increases from 12.04% to 19.32%, and C=O and O–C=O increase to 4.13% and 6.52%, respectively. The total oxygen-containing carbon fraction increases from 18.28% to 29.97%. Under CO_2, C–C/C–H in FS char further decreases to 68.35%, while C=O and O–C=O increase to 5.91% and 7.41%, respectively, and the total oxygen-containing carbon fraction reaches 31.65%. These results suggest that the CO_2 atmosphere promotes the formation or preservation of more oxidized carbon structures, such as carbonyl and carboxyl groups, on the FS char surface.

For CJ, the changes in surface carbon structure are more pronounced. Under N_2, the C–C/C–H fraction decreases from 88.10% in the raw sample to 68.13%, whereas C–O/C–OH increases from 8.03% to 20.43%. The C=O and O–C=O fractions also increase to 4.48% and 6.97%, respectively, raising the total oxygen-containing carbon fraction from 11.82% to 31.88%. Under CO_2, the C–C/C–H fraction further decreases to 65.44%, while C–O/C–OH, C=O, and O–C=O increase to 22.12%, 5.02%, and 7.42%, respectively. The total oxygen-containing carbon fraction reaches 34.56%, indicating that CJ is more sensitive to CO_2-involved gas–solid reactions than FS.

Overall, pyrolysis shifts the surface carbon structure of both oil shales from C–C/C–H-dominated species toward oxygen-containing carbon species. Compared with N_2, CO_2 increases the total oxygen-containing carbon fraction on both char surfaces, especially the more highly oxidized C=O and O–C=O components. However, the change in C–O/C–OH is sample-dependent: it is slightly lower in FS-CO_2 than in FS-N_2, but higher in CJ-CO_2 than in CJ-N_2. These results suggest that CO_2 mainly promotes the formation or preservation of more oxidized carbon structures rather than uniformly increasing all oxygen-containing groups.

3.5. Evolution of Pore Structure and Micro-Morphology During Pyrolysis

3.5.1. BET Pore Structure and N_2 Adsorption–Desorption Characteristics

Figure 10 shows the N_2 adsorption–desorption isotherms of raw FS and CJ oil shales and their chars obtained under N_2 and CO_2 atmospheres. Overall, all samples exhibit distinct hysteresis loops in the medium- to high-relative-pressure region. The isotherms are close to type IV with H3-type hysteresis loops as defined by IUPAC, indicating that the pores are mainly slit-shaped mesopores formed by the stacking of plate-like particles, with some macropores also present [21,22]. After pyrolysis, the adsorption capacity of both chars increases in the low- to medium-relative-pressure region, and the hysteresis loops become wider. This indicates that volatile release, organic-matter shrinkage, and framework rearrangement jointly promote pore generation and pore-channel connectivity.

Table 6 further summarizes the specific surface area and average pore diameter of the samples. For the raw oil shales, FS showed a specific surface area of 10.5273 $m^2 \cdot g^{-1}$, which was markedly higher than that of CJ at 3.2015 $m^2 \cdot g^{-1}$. The average pore diameter of FS is 12.8450 nm, smaller than the 18.3821 nm of CJ. This indicates that raw FS contains more smaller mesopores, whereas raw CJ is dominated by mesopores with a larger average pore diameter and shows weaker overall pore development. This difference may be related to the mineral framework, organic-matter occurrence, and ash composition of the two oil shales. Figure 11 further shows that, under N_2, the pore-size distributions of both chars shift toward the mesopore/small-pore region, indicating that volatile release opens original closed pores and forms new pores. Under CO_2, the contribution of small pores weakens in FS, whereas the pore-size distribution of CJ shifts markedly toward smaller pore diameters, suggesting different pore-restructuring effects of CO_2 on the two chars. This observation agrees with the pronounced decrease in specific surface area for FS-CO_2 and the substantial reduction in average pore diameter for CJ-CO_2, as summarized in Table 5.

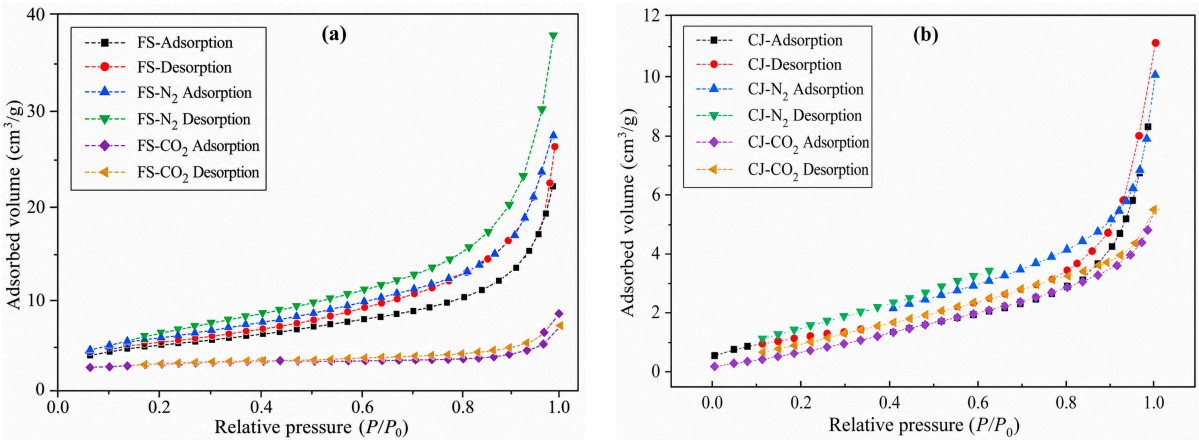


Figure 10. N_2 adsorption–desorption isotherms of raw FS and CJ oil shales and their pyrolysis chars: (**a**) FS samples; (**b**) CJ samples.

Table 6. Specific surface area and average pore diameter of FS and CJ oil shales and their pyrolysis chars.

Sample	FS	FS-N_2	FS-CO_2	CJ	CJ-N_2	CJ-CO_2
Specific surface area ($m^2 \cdot g^{-1}$)	10.5273	14.1402	2.7783	3.2015	6.1464	4.4063
Average pore diameter (nm)	12.8450	14.1653	15.5209	18.3821	8.6766	5.9811

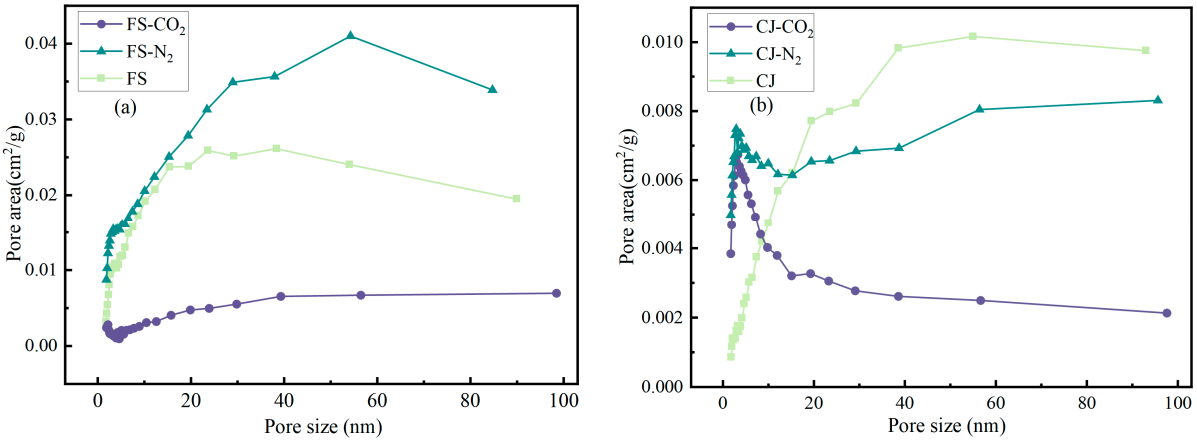


Figure 11. Pore size distributions of raw FS and CJ oil shales and their pyrolysis chars: (**a**) FS samples; (**b**) CJ samples.

Pyrolysis under N_2 significantly promotes pore development in both oil shales. The specific surface area of FS-N_2 rose to 14.1402 $m^2 \cdot g^{-1}$, approximately 34.3% higher than that of raw FS, while the average pore diameter increased only slightly, from 12.8450 to 14.1653 nm. This indicates that volatile release during N_2 pyrolysis opens closed pores and generates a new mesopore network while largely maintaining the original mesopore scale. For CJ-N_2, the specific surface area rose from 3.2015 to 6.1464 $m^2 \cdot g^{-1}$, corresponding to an increase of approximately 92.0%, whereas the average pore diameter decreased from 18.3821 to 8.6766 nm. This suggests that numerous smaller pores are generated during CJ pyrolysis under N_2, and that the original larger pores are refined or divided, shifting the pore-size distribution toward smaller pores.

Under CO_2, the two oil shales show clearly different pore evolution behaviors. For FS, the specific surface area decreased to 2.7783 $m^2 \cdot g^{-1}$ in the CO_2-derived char, which was approximately 73.6% lower than that of raw FS and 80.4% lower than that of FS-N_2. Its average pore diameter increases to 15.5209 nm, higher than those of both raw FS and FS-N_2. This suggests that some mesopores and small pores in FS may be blocked, merged, or covered by ash during CO_2 pyrolysis, leading to a substantial loss of effective surface area, while the remaining pores shift toward larger diameters. For CJ, the specific surface area of CJ-CO_2 increases from 3.2015 to 4.4063 $m^2 \cdot g^{-1}$, an increase of about 37.6%, but remains lower than the 6.1464 $m^2 \cdot g^{-1}$ of CJ-N_2. Its average pore diameter decreases sharply from 18.3821 to 5.9811 nm, indicating that CO_2 also promotes the formation of smaller pores, although the pore-network connectivity is less developed than under N_2. Similar atmosphere-dependent pore evolution has also been reported for oil shale and other carbonaceous solid fuels. CO_2 can participate in char conversion through gasification reactions, which may promote pore generation and modify the pore structure of residual chars [8,12,13]. However, the opposite trend observed for FS char in the present study suggests that the mineral-rich nature of oil shale can significantly modify the effect of CO_2. The migration and redistribution of inorganic components during pyrolysis may result in ash-shell formation and pore-mouth blockage, which can offset the pore-opening effect induced by CO_2 gasification [3,22,23]. This difference highlights the importance of considering mineral composition when evaluating the CO_2-induced structural evolution of oil shale chars.

These results suggest that N_2 better promotes the development of a well-connected mesopore–small-pore system, as both chars reached their highest specific surface areas in the N_2 atmosphere. In contrast, CO_2 has a pronounced pore-structure passivation effect on FS, significantly decreasing its specific surface area and increasing its average pore

diameter. For CJ, CO_2 mainly causes pore refinement and small-pore formation, but the increase in specific surface area is limited. This suggests that CO_2-involved gas–solid reactions, carbonate-related decomposition, and ash rearrangement have dual effects: they may promote new pore formation through gasification and devolatilization, but may also reduce effective pore connectivity through ash coverage, pore-mouth blockage, or mineral agglomeration. Such differences in pore structure are expected to influence the diffusion of O_2/CO_2 into particles and the accessible reaction interfacial area during subsequent combustion or gasification. These BET and N_2 adsorption–desorption results provide quantitative pore-structure information and were further combined with SEM observations to interpret the atmosphere-dependent morphological evolution of the chars.

3.5.2. SEM Micro-Morphology Analysis

Figure 12 shows the SEM images of raw FS and CJ oil shales and their pyrolysis chars. To avoid relying only on local morphological observations, the SEM features were interpreted together with the BET specific surface area, average pore diameter, and N_2 adsorption–desorption results. Raw FS and CJ particles are generally dense, with surfaces mainly composed of irregular blocky or flaky structures. Macroscopic pores are limited, and only small local cracks are observed, indicating that organic matter is mainly embedded within a dense mineral matrix before pyrolysis. Combined with the BET results, raw FS has a relatively high specific surface area of 10.5273 $m^2 \cdot g^{-1}$, but its pores are mainly smaller mesopores. Raw CJ has a specific surface area of only 3.2015 $m^2 \cdot g^{-1}$ and a larger average pore diameter of 18.3821 nm, indicating fewer pores but relatively larger pore sizes. SEM morphology and BET parameters together show that both raw oil shales are strongly constrained by the mineral framework, although their pore-development degree and average pore size differ.

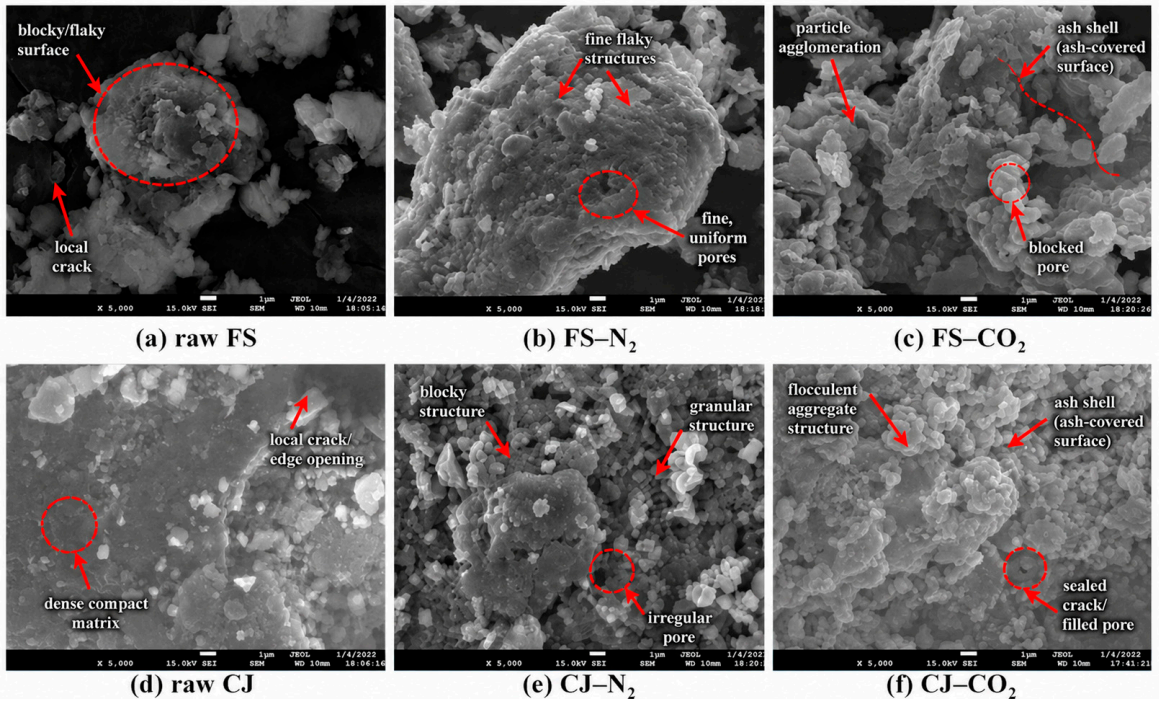


Figure 12. SEM images of raw FS and CJ oil shales and their pyrolysis chars obtained under N_2 and CO_2 atmospheres: (**a**) raw FS, (**b**) FS–N_2, (**c**) FS–CO_2, (**d**) raw CJ, (**e**) CJ–N_2, and (**f**) CJ–CO_2. Arrows and circles indicate the main morphological features discussed in the text. Magnification: ×5000.

After pyrolysis under N_2, char particles from both samples show clear fragmentation, shrinkage, crack extension, and increased pore development. These morphological changes

are consistent with the N_2 adsorption–desorption results, which show enhanced adsorption capacity and wider hysteresis loops after pyrolysis. FS–N_2 consists of finer particles and flaky structures, with smaller and more uniformly distributed pores, corresponding to the increase in specific surface area from 10.5273 to 14.1402 $m^2 \cdot g^{-1}$. CJ–N_2 exhibits coexisting blocky and granular structures, with cracks along the bedding direction and irregular pores. Its specific surface area increased from 3.2015 to 6.1464 $m^2 \cdot g^{-1}$, whereas the average pore diameter decreased from 18.3821 to 8.6766 nm. This indicates that volatile release and framework shrinkage not only generated new pores but also subdivided larger original pores into smaller mesopores.

Under CO_2, the char morphologies differ more markedly. FS–CO_2 particles tend to agglomerate, and some surface pores are covered by ash, forming a thin ash shell over the porous framework. This SEM observation explains the BET result that the specific surface area of FS–CO_2 decreases to 2.7783 $m^2 \cdot g^{-1}$ and the average pore diameter increases to 15.5209 nm. These changes indicate that ash-shell coverage, pore-mouth blockage, and possible small-pore coalescence reduce the effective surface area. CJ–CO_2 char forms expanded blocky or flocculent aggregates with a denser and more continuous ash shell, and some original pores and cracks are filled or sealed. However, its average pore diameter decreases from 18.3821 to 5.9811 nm, indicating that CO_2 still promotes small-pore formation and pore-size refinement despite local ash-shell coverage.

The SEM and BET results together indicate that pyrolysis generally promotes the transformation of both oil shales from dense blocks into porous char frameworks, while the atmosphere controls the relative balance between pore formation and pore blockage. Under N_2, pyrolysis is mainly governed by devolatilization and solid-phase shrinkage, resulting in more sufficient pore generation. Under CO_2, gas–solid reactions, carbonate-related decomposition, and ash migration act together; they may create new pores but can also cause ash-shell coverage and particle agglomeration. For subsequent combustion or gasification, cracks and pores facilitate gas diffusion and increase the reaction interface, whereas ash-shell coverage and pore closure may form mass-transfer barriers. Therefore, char morphological evolution should be evaluated in combination with specific surface area, average pore diameter, and pore-size distribution, rather than assessing reactivity solely from local SEM observations.

During pyrolysis, mineral components do not remain completely unchanged. Silicate minerals mainly maintain the inorganic skeleton, while clay-related minerals may undergo dehydration and structural rearrangement. Ca/Mg-bearing minerals may experience carbonate-related transformation at elevated temperatures. The migration and redistribution of these inorganic phases may either promote pore generation or cause ash-shell coverage and pore blockage, depending on the sample composition and atmosphere. Recent studies have further indicated that inorganic components and carbon structural ordering can jointly influence the subsequent reactivity of oil shale chars. In particular, CaO- and Fe_2O_3-containing mineral components may promote char conversion through catalytic effects, whereas an increase in the ordering degree of the residual carbon structure may reduce reaction accessibility and conversion rates [42]. These findings support the interpretation that the final behavior of oil shale char depends on the combined effects of pore accessibility, carbon structural characteristics, and mineral redistribution. However, because Raman characterization and direct char combustion/gasification reactivity tests were not performed in the present study, this interpretation should be regarded as a mechanistic inference rather than direct experimental validation. Although FTIR, XPS, BET, SEM, and XRF provide complementary information on functional groups, surface carbon species, pore structure, morphology, and ash oxide composition, these techniques do not fully determine the functional surface properties or crystalline mineral phases of the chars.

3.6. Proposed Pyrolysis Mechanism Under N_2 and CO_2 Atmospheres

Based on the TG–DTG results, char-structure characterization, and kinetic analysis, a simplified mechanism of oil shale pyrolysis under N_2 and CO_2 atmospheres is proposed in Figure 13. Under N_2, the atmosphere mainly acts as an inert carrier gas. The pyrolysis process is dominated by kerogen cracking, volatile release, tar or shale-oil precursor formation, and residual char formation. The release of volatiles promotes fragmentation, shrinkage, crack extension, and pore development, resulting in a porous char framework with a relatively higher specific surface area.

Under CO_2, the pyrolysis mechanism is more complex. In the early stage, the higher heat capacity and lower thermal diffusivity of CO_2 cause thermal buffering and heat-transfer delay, which postpones volatile release and reduces the apparent mass-loss rate. At medium and high temperatures, CO_2 may participate in char gasification through the reaction Char-C + CO_2 → 2CO. Meanwhile, carbonate-related transformation, ash migration, and mineral–char interactions may contribute to pore restructuring. These coupled effects can generate new pores but may also cause ash-shell coverage, pore-mouth blockage, particle agglomeration, and filled or sealed pores. Therefore, CO_2 delays the macroscopic pyrolysis process but can still modify the char structure and introduce additional reaction pathways at medium and high conversion levels.

The proposed pathways are broadly consistent with recent integrated studies linking kerogen bond cleavage, mineral composition, gas evolution, product distribution, and char conversion with pyrolysis temperature and heating history [8,24,26]. However, the relative importance of these pathways remains sample-dependent because of differences in organic structure, inorganic composition, and pore evolution. Because the liquid and gaseous products and in situ mineral-phase evolution were not directly measured in the present study, the proposed mechanism should be regarded as a mechanistic framework rather than a complete reaction network. The reactions shown in Figure 13 are therefore schematic pathways rather than strict overall stoichiometric reactions.

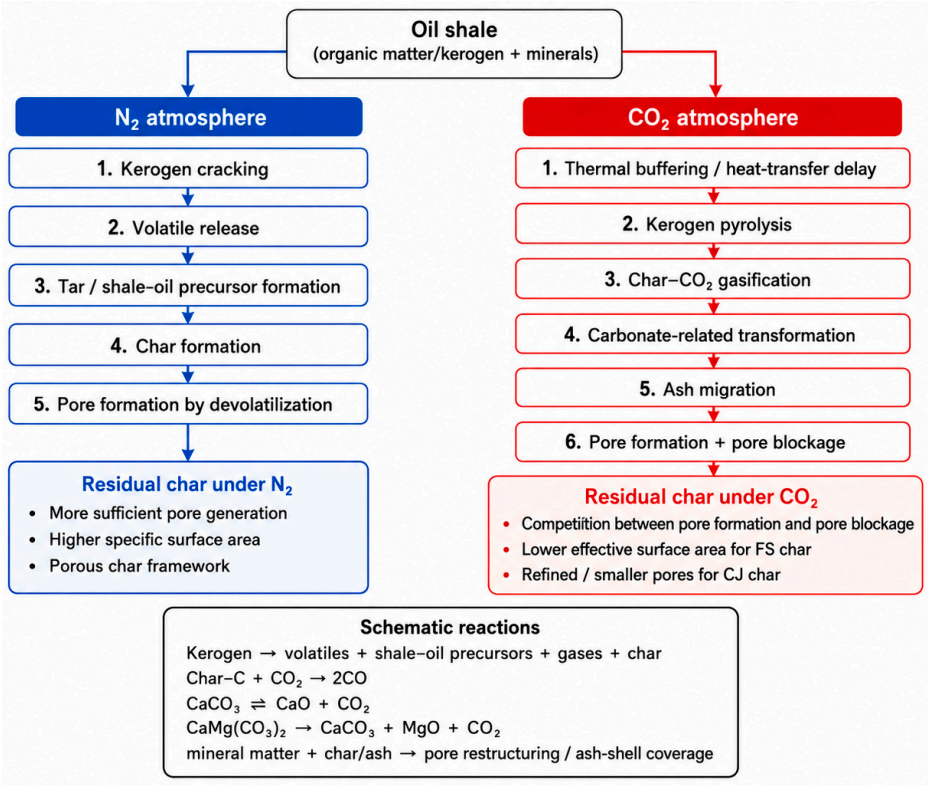


Figure 13. Schematic mechanism of oil shale pyrolysis under N_2 and CO_2 atmospheres.

4. Conclusions

In this study, Fushun and Changji oil shales were selected to systematically compare their pyrolysis behavior, char structural evolution, and kinetic characteristics under N_2 and CO_2 atmospheres. This objective was achieved by establishing the relationships among atmospheric effects, mineral composition, char structural evolution, and kinetic response for two representative oil shales. The main conclusions are as follows:

(1) Both FS and CJ oil shales exhibited high ash contents, low fixed-carbon contents, and low heating values. CJ showed a slightly higher carbon content and HHV than FS, indicating relatively greater organic-matter enrichment and heat-release potential. XRF analysis further showed that both FS and CJ ashes were dominated by SiO_2, while FS ash contained higher Al_2O_3 and Fe_2O_3 contents and CJ ash contained much higher CaO and MgO contents. These differences in inorganic composition provide a basis for interpreting the more pronounced high-temperature mineral-related mass loss and stronger atmosphere-dependent structural response of CJ oil shale, highlighting the important role of mineral composition in controlling CO_2-induced pyrolysis behavior.

(2) TG–DTG results showed that both oil shales underwent three main stages under N_2 and CO_2 atmospheres: moisture release, main organic-matter pyrolysis, and high-temperature mineral decomposition/transformation. Increasing the heating rate from 5 to 40 °C·min^{-1} shifted T_s and T_{max} toward higher temperatures and increased the maximum mass-loss rate and volatile-release characteristic index, indicating that rapid heating intensified the concentrated release of volatiles. Compared with N_2, CO_2 delayed the onset of pyrolysis and made volatile release more gradual. At 40 °C·min^{-1}, replacing N_2 with CO_2 increased T_s from 322.6 to 399.3 °C for FS and from 368.1 to 377.3 °C for CJ, while reducing the maximum mass-loss rates to 6.81 and 8.66%·min^{-1}, respectively.

(3) FTIR observations and XPS C 1s peak-fitting results indicated that pyrolysis weakened aliphatic C–H structures and enriched aromatic/carbonaceous frameworks in the residual chars. CO_2 promoted the formation or preservation of oxygen-containing surface carbon species, especially C=O and O–C=O groups. BET and SEM results further showed that N_2 was more favorable for pore development, increasing the specific surface areas of FS and CJ chars to 14.1402 and 6.1464 m^2·g^{-1}, respectively. In contrast, CO_2 caused ash-shell coverage, pore-mouth blockage, and particle agglomeration in FS char, reducing its specific surface area to 2.7783 m^2·g^{-1}, while promoting pore-size refinement and smaller-pore formation in CJ char. These atmosphere-dependent structural changes may further influence gas diffusion, reactive surface area, and char reactivity during subsequent combustion or gasification processes.

(4) The apparent activation energy E_α calculated by the Friedman, FWO, KAS, Starink, and Vyazovkin iso-conversional methods generally showed a trend of first decreasing and then increasing with conversion. The activation energies were generally lower under CO_2 than under N_2. The average activation-energy differences between the two atmospheres were 23.5 and 43.2 kJ·mol^{-1} for FS and CJ, respectively, indicating that CJ was more sensitive to atmosphere switching. This difference is likely associated with the combined effects of char–CO_2 gasification, carbonate-related transformation, ash migration, and pore restructuring at medium and high conversions.

(5) The proposed schematic mechanism in Figure 11 suggests that N_2 mainly promotes devolatilization-dominated pore development, whereas CO_2 may exert combined thermal-buffering, char-gasification, carbonate-related transformation, and ash-migration effects. These coupled processes contribute to the delayed mass loss, modified char structure, and lower apparent activation energy observed under CO_2. The present findings provide practical implications for the design and modeling of

CO_2-rich thermal conversion and oxy-fuel processes, indicating that both atmospheric characteristics and mineral composition should be considered when predicting oil shale conversion behavior. However, this study was conducted under laboratory-scale thermogravimetric and fixed-bed pyrolysis conditions. The effects of reactor hydrodynamics, particle-scale heat transfer, and long-term mineral evolution under industrial conditions require further investigation.

Supplementary Materials: The following supporting information can be downloaded at: https://www.mdpi.com/article/10.3390/pr14152439/s1, Figure S1: Representative Starink linear fitting for FS oil shale pyrolysis under N_2 at α = 0.50; Table S1: Processed TG data and Starink variables for FS oil shale pyrolysis under N_2 at α = 0.50.

Author Contributions: Conceptualization, Q.L., Q.W., J.B., C.X.; methodology, Q.L.; software, Q.L., Z.W.; validation, Q.L., Q.W., J.B., S.G., C.X.; formal analysis, Q.L., Z.W., S.G.; investigation, Q.L., Z.W.; resources, Q.W., J.B.; data curation, Q.L., Z.W.; writing—original draft preparation, Q.L., Z.W.; writing—review and editing, Q.W., J.B., S.G., C.X.; visualization, Q.L., Z.W.; supervision, Q.W., J.B., C.X.; project administration, Q.W., J.B.; funding acquisition, Q.W., J.B. All authors have read and agreed to the published version of the manuscript.

Funding: This research was funded by Jilin Provincial Science and Technology Development Plan Project (20210203202SF), the National Natural Science Foundation of China (No. 52476106), the Natural Science Foundation of Jilin Province, China (YDZJ20241570ZTTS), Scientific Research Project of Education Department of Jilin Province, China (JJKH20261245KJ) and the Natural Science Foundation of Inner Mongolia Autonomous Region, China (2025MS05039).

Data Availability Statement: The original contributions presented in this study are included in the article. Further inquiries can be directed to the corresponding author.

Conflicts of Interest: The authors declare no conflicts of interest.

References

1. Qian, J.; Yin, L.; Wang, J. *Oil Shale: A Supplementary Energy Source to Petroleum*; China Petrochemical Press: Beijing, China, 2008. (In Chinese)
2. Dyni, J.R. *Geology and Resources of Some World Oil-Shale Deposits*; U.S. Geological Survey Scientific Investigations Report 2005–5294; U.S. Geological Survey: Reston, VA, USA, 2006; p. 42.
3. Jiang, X.M.; Han, X.X.; Cui, Z.G. Progress and recent utilization trends in combustion of Chinese oil shale. *Prog. Energy Combust. Sci.* **2007**, *33*, 552–579. [CrossRef]
4. Jiang, X.M.; Han, X.X.; Cui, Z.G. New technology for the comprehensive utilization of Chinese oil shale resources. *Energy* **2007**, *32*, 772–777. [CrossRef]
5. Lu, Y.; Wang, Y.; Zhang, J.; Zhao, Y.; Li, G.; Zhang, Y. Combustion characteristics of Xinjiang Changji oil shale blended with coal. *Therm. Power Gener.* **2019**, *48*, 21–26. (In Chinese)
6. Ma, Y.; Xiang, Q.Y.; Ding, K.L. Development of oil shale at home and abroad. *World Pet. Ind.* **2024**, *31*, 16–25. (In Chinese)
7. Wang, Q.; Liu, Q.; Wang, Z.C.; Liu, H.P.; Bai, J.R.; Ye, J.B. Characterization of organic nitrogen and sulfur in the oil shale kerogens. *Fuel Process. Technol.* **2017**, *160*, 170–177. [CrossRef]
8. Yang, S.; Wang, H.; Zheng, J.; Pan, Y.; Ji, C. Comprehensive review: Study on heating rate characteristics and coupling simulation of oil shale pyrolysis. *J. Anal. Appl. Pyrolysis* **2024**, *177*, 106289. [CrossRef]
9. Pan, Y.; Peng, J.; Yang, S.; Fu, J.; Li, L. Review of electric heating technology of oil shale and its simulation. *J. Anal. Appl. Pyrolysis* **2023**, *175*, 106205. [CrossRef]
10. Wang, L.; Gao, C.H.; Xiong, R.Y.; Zhang, X.J.; Guo, J.X. Development review and the prospect of oil shale in situ catalysis conversion technology. *Pet. Sci.* **2024**, *21*, 1385–1395. [CrossRef]
11. Xie, F.F.; Wang, Z.; Lin, W.G.; Song, W.L. Study on thermal conversion of Huadian oil shale under N_2 and CO_2 atmospheres. *Oil Shale* **2010**, *27*, 309–320. [CrossRef]
12. Kok, M.V. Thermal investigation of Seyitömer oil shale. *Thermochim. Acta* **2001**, *369*, 149–155. [CrossRef]
13. Burnham, A.K.; Braun, R.L. Global kinetic analysis of complex materials. *Energy Fuels* **1999**, *13*, 1–22.

14. Zhao, S.; Sun, Y.; Lü, X.; Li, Q. Kinetics and thermodynamics evaluation of carbon dioxide enhanced oil shale pyrolysis. *Sci. Rep.* **2021**, *11*, 516. [CrossRef] [PubMed]
15. Buhre, B.J.P.; Elliott, L.K.; Sheng, C.D.; Gupta, R.P.; Wall, T.F. Oxy-fuel combustion technology for coal-fired power generation. *Prog. Energy Combust. Sci.* **2005**, *31*, 283–307. [CrossRef]
16. Toftegaard, M.B.; Brix, J.; Jensen, P.A.; Glarborg, P.; Jensen, A.D. Oxy-fuel combustion of solid fuels. *Prog. Energy Combust. Sci.* **2010**, *36*, 581–625. [CrossRef]
17. Liu, Q.; Wang, Q.; Wang, Z.; Di, H. Influence of CO_2 substitution for N_2 on the combustion characteristics and kinetics of oil shale under oxy-fuel conditions. *RSC Adv.* **2025**, *15*, 37937–37950. [CrossRef] [PubMed]
18. Kang, Z.; Wang, Z.; Lu, Y.; Cao, R.; Huang, D.; Meng, Q. Investigation on the effect of atmosphere on the pyrolysis behavior and oil quality of Jimusar oil shale. *Geofluids* **2022**, *2022*, 1408690. [CrossRef]
19. Huang, D.; Kang, Z.; Yang, D.; Cao, R.; Cui, Z.; Lu, Y. Study on the pyrolysis behavior and kinetics of Jimusar oil shale with H_2O/CO_2 injection. *Oil Shale* **2023**, *40*, 321–343. [CrossRef]
20. Chen, B.; Han, X.; Jiang, X. In situ FTIR analysis of the evolution of functional groups of oil shale during pyrolysis. *Energy Fuels* **2016**, *30*, 5611–5616. [CrossRef]
21. Han, J.; Sun, Y.; Guo, W.; Li, Q.; Deng, S. Characterization of pyrolysis of Nong'an oil shale at different temperatures and analysis of pyrolysate. *Oil Shale* **2019**, *36*, 151–170. [CrossRef]
22. Pikkor, H.; Lees, H.; Maaten, B.; Järvik, O.; Konist, A. Surface characterisation of Estonian oil shale semi-coke. *Chem. Eng. Trans.* **2020**, *81*, 853–858.
23. Tiwari, P.; Deo, M.; Lin, C.L.; Miller, J.D. Characterization of oil shale pore structure before and after pyrolysis by using X-ray micro CT. *Fuel* **2013**, *107*, 547–554. [CrossRef]
24. Wang, Q.; Wang, X.; Pan, S. Study on the structure, pyrolysis kinetics, gas release, reaction mechanism, and pathways of Fushun oil shale and kerogen in China. *Fuel Process. Technol.* **2022**, *225*, 107058. [CrossRef]
25. Zhang, J.; Ding, Y.; Du, W.; Lu, K.; Sun, L. Study on pyrolysis kinetics and reaction mechanism of Beizao oil shale. *Fuel* **2021**, *296*, 120696. [CrossRef]
26. Zhao, F.; Yang, Z.; Zhang, L.; Zhang, C.; Wang, T.; Zhang, H. The effect of temperature on pyrolysis products during oil shale thermal decomposition. *Sci. Rep.* **2025**, *15*, 26135. [CrossRef] [PubMed]
27. Friedman, H.L. Kinetics of thermal degradation of char-forming plastics from thermogravimetry. Application to a phenolic plastic. *J. Polym. Sci. C Polym. Symp.* **1964**, *6*, 183–195. [CrossRef]
28. Flynn, J.H.; Wall, L.A. A quick, direct method for the determination of activation energy from thermogravimetric data. *J. Polym. Sci. B Polym. Lett.* **1966**, *4*, 323–328. [CrossRef]
29. Ozawa, T. A new method of analyzing thermogravimetric data. *Bull. Chem. Soc. Jpn.* **1965**, *38*, 1881–1886. [CrossRef]
30. Kissinger, H.E. Reaction kinetics in differential thermal analysis. *Anal. Chem.* **1957**, *29*, 1702–1706. [CrossRef]
31. Starink, M.J. The determination of activation energy from linear heating rate experiments: A comparison of the accuracy of isoconversion methods. *Thermochim. Acta* **2003**, *404*, 163–176. [CrossRef]
32. Vyazovkin, S.; Burnham, A.K.; Criado, J.M.; Pérez-Maqueda, L.A.; Popescu, C.; Sbirrazzuoli, N. ICTAC Kinetics Committee recommendations for performing kinetic computations on thermal analysis data. *Thermochim. Acta* **2011**, *520*, 1–19. [CrossRef]
33. Akahira, T.; Sunose, T. Method of determining activation deterioration constant of electrical insulating materials. *Res. Rep. Chiba Inst. Technol. Sci. Technol.* **1971**, *16*, 22–31.
34. Vyazovkin, S. Model-free kinetics: Staying free of multiplying entities without necessity. *J. Therm. Anal. Calorim.* **2006**, *83*, 45–51. [CrossRef]
35. Chi, M.; Xu, X.; Cui, D.; Zhang, H.; Wang, Q. A TG–FTIR investigation and kinetic analysis of oil shale kerogen pyrolysis using the distributed activation energy model. *Oil Shale* **2016**, *33*, 228–247. [CrossRef]
36. Vyazovkin, S.; Dollimore, D. Linear and nonlinear procedures in isoconversional computations of the activation energy of nonisothermal reactions in solids. *J. Chem. Inf. Comput. Sci.* **1996**, *36*, 42–45. [CrossRef]
37. Vyazovkin, S. Evaluation of activation energy of thermally stimulated solid-state reactions under arbitrary variation of temperature. *J. Comput. Chem.* **1997**, *18*, 393–402. [CrossRef]
38. Vyazovkin, S. Modification of the integral isoconversional method to account for variation in the activation energy. *J. Comput. Chem.* **2001**, *22*, 178–183.
39. Loo, L.; Maaten, B.; Siirde, A.; Pihu, T.; Konist, A. Experimental analysis of the combustion characteristics of Estonian oil shale in air and oxy-fuel atmospheres. *Fuel Process. Technol.* **2015**, *134*, 317–324. [CrossRef]
40. Liu, B.-S.; Yao, C.-J.; Qi, J.-L.; Liu, Y.-Q.; Xu, L.; Hou, J.-X. Experimental investigation on pyrolysis products and pore structure characteristics of organic-rich shale heated by supercritical carbon dioxide. *Pet. Sci.* **2024**, *21*, 2393–2406. [CrossRef]

41. Biniak, S.; Szymański, G.; Siedlewski, J.; Świątkowski, A. The characterization of activated carbons with oxygen and nitrogen surface groups. *Carbon* **1997**, *35*, 1799–1810. [CrossRef]
42. Yan, Y.; Gao, H.; Sui, Y.; Hu, Z.; Han, Z.; Xu, G. The catalytic effect of inner minerals on the combustion of oil shale char: Characteristics and mechanism. *Fuel Process. Technol.* **2022**, *236*, 107426. [CrossRef]

Disclaimer/Publisher's Note: The statements, opinions and data contained in all publications are solely those of the individual author(s) and contributor(s) and not of MDPI and/or the editor(s). MDPI and/or the editor(s) disclaim responsibility for any injury to people or property resulting from any ideas, methods, instructions or products referred to in the content.